AGU PUBLICATIONS

Tectonics

RESEARCH ARTICLE
10.1002/2016TC004258

Key Points:
- The Himalayan foreland basin sediments of the Siwalik Group exposed at Dungsam Chu (eastern Bhutan) were deposited between 7 and 1 Ma
- The orographic effect of the Shillong Plateau had a limited impact on the wet paleoclimate of the Bhutanese foothills in the Pliocene
- Plio-Pleistocene slowdown of deformation on the MBT results from partitioning of the India-Eurasia convergence into the Shillong Plateau

Supporting Information:
- Supporting Information S1

Correspondence to:
I. Coutand,
icoutand@dal.ca

Citation:
Coutand, I., L. Barrier, G. Govin, D. Grujic, C. Hoorn, G. Dupont-Nivet, and Y. Najman (2016), Late Miocene-Pleistocene evolution of India-Eurasia convergence partitioning between the Bhutan Himalaya and the Shillong Plateau: New evidences from foreland basin deposits along the Dungsam Chu section, eastern Bhutan, *Tectonics*, *35*, 2963–2994, doi:10.1002/2016TC004258.

Received 27 MAY 2016
Accepted 17 OCT 2016
Accepted article online 28 OCT 2016
Published online 17 DEC 2016

Late Miocene-Pleistocene evolution of India-Eurasia convergence partitioning between the Bhutan Himalaya and the Shillong Plateau: New evidences from foreland basin deposits along the Dungsam Chu section, eastern Bhutan

Isabelle Coutand[1], Laurie Barrier[2], Gwladys Govin[3], Djordje Grujic[1], Carina Hoorn[4], Guillaume Dupont-Nivet[5], and Yani Najman[3]

[1]Department of Earth Sciences, Dalhousie University, Halifax, Nova Scotia, Canada, [2]Institut de Physique du Globe de Paris, Sorbonne Paris Cité, Université Paris Diderot, UMR 7154 CNRS, Paris, France, [3]Lancaster Environment Centre, University of Lancaster, Lancaster, UK, [4]Institute for Biodiversity and Ecosystem Dynamics, University of Amsterdam, Amsterdam, Netherlands, [5]Géosciences Rennes UMR-CNRS 6118, Rennes, France

Abstract The Shillong Plateau is a unique basement-cored uplift in the foreland of the eastern Himalaya that accommodates part of the India-Eurasia convergence since the late Miocene. It was uplifted in the late Pliocene to 1600 m, potentially inducing regional climatic perturbations by orographically condensing part of the Indian Summer Monsoon (ISM) precipitations along its southern flank. As such, the eastern Himalaya-Shillong Plateau-ISM is suited to investigate effects of tectonics, climate, and erosion in a mountain range-broken foreland system. This study focuses on a 2200 m thick sedimentary section of the Siwalik Group strategically located in the lee of the Shillong Plateau along the Dungsam Chu at the front of the eastern Bhutan Himalaya. We have performed magnetostratigraphy constrained by vitrinite reflectance and detrital apatite fission track dating, combined with sedimentological and palynological analyses. We show that (1) the section was deposited between ~7 and 1 Ma in a marginal marine deltaic transitioning into continental environment after 5 Ma, (2) depositional environments and paleoclimate were humid with no major change during the depositional period indicating that the orographic effect of the Shillong Plateau had an unexpected limited impact on the paleoclimate of the Bhutanese foothills, and (3) the diminution of the flexural subsidence in the basin and/or of the detrital input from the range is attributable to a slowdown of the displacement rates along the Main Boundary Thrust in eastern Bhutan during the latest Miocene-Pleistocene, in response to increasing partitioning of the India-Eurasia convergence into the active faults bounding the Shillong Plateau.

1. Introduction

Sedimentary archives of the Neogene-Quaternary Siwalik Group preserved in the Himalayan foreland basin have been extensively documented along the Himalayan arc from Pakistan to Nepal, providing valuable information on mountain building in space and time, past organization of drainage networks, and paleoclimate [e.g., *Najman*, 2006, and references therein]. Recent studies have also focused on sections of the Siwalik Group in eastern India, in the states of West Bengal [*More et al.*, 2016] and Arunachal Pradesh [*Chirouze et al.*, 2012, 2013; *Lang et al.*, 2016]; however, there is still a lack of information in the frontal Bhutan Himalaya, leaving about 400 km along the strike of the orogen of undocumented foreland basin deposits regarding ages, thicknesses, sedimentary facies, and depositional paleoenvironments.

Bhutan is located directly north of the Shillong Plateau, the only raised topography in the foreland of the Himalayas (Figure 1), which corresponds to a 1600 m high ancient erosion surface tilted northward by 2–4° [*Biswas et al.*, 2007; *Clark and Bilham*, 2008]. This plateau is made of Proterozoic-Paleozoic basement [*Chatterjee et al.*, 2007; *Ghosh et al.*, 1994; *Mitra and Mitra*, 2001; *Selvam et al.*, 1995; *Yin et al.*, 2010], uplifted along steep and seismically active crustal-scale reverse faults: the E-W trending Dauki Fault in the south and the inferred WNW-ESE trending Oldham Fault in the north [*Bilham and England*, 2001; *Biswas and Grasemann*, 2005; *Mitra et al.*, 2005; *Rajendran et al.*, 2004] (Figure 1). The Shillong Plateau is bounded to

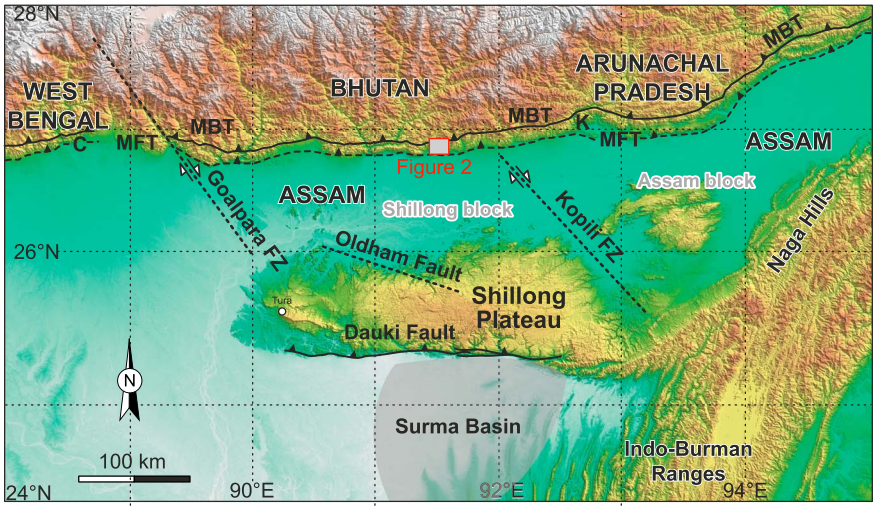

Figure 1. Digital topography and major structural features of southern Bhutan and Shillong Plateau area. Elevation data are from Shuttle Radar Topography Mission 3 data (U.S. Geological Survey). Structural data are from *Gansser* [1983], *Biswas and Grasemann* [2005], and *Hirschmiller et al.* [2014]. The light shaded area south of the Shillong Plateau represents the location of the Surma Basin after *Najman et al.* [2016]. Abbreviations are MBT: Main Boundary Thrust, MFT: Main Frontal Thrust, C: Churanthi river section [*More et al.*, 2016], and K: Kameng section [*Chirouze et al.*, 2012, 2013].

the east by a NW-SE trending shear zone, the Kopili fracture zone [*Kayal et al.*, 2010], accommodating right-lateral displacement at a rate of 3 mm/yr through the differential clockwise rotation between the Assam and Shillong blocks [*Vernant et al.*, 2014]; to the west it is marked by the NW-SE trending Goalpara right-lateral shear zone [*Diehl et al.*, 2016]. At the longitude of central and eastern Bhutan, the Himalayan foreland corresponds to a "broken foreland basin" [e.g., *Jordan*, 1995; *Strecker et al.*, 2012], with a foredeep that may be $<$1 km thick, in contrast to areas west and east of Bhutan where the Brahmaputra/Ganges foredeep reaches depths $>$4 km [*Dasgupta*, 2000; *Verma and Mukhopadhyay*, 1977; *Vernant et al.*, 2014, Figure 1b]. On the Dauki Fault at the southern front of the Shillong, horizontal displacement averaged over the last 9–15 Ma was estimated at 0.65–2.3 mm/yr [*Biswas et al.*, 2007] or 1–2.9 mm/yr [*Clark and Bilham*, 2008], while GPS data indicate much faster modern rates increasing eastward from 3 to 7 mm/yr [*Vernant et al.*, 2014], suggesting that the amount of India-Eurasia convergence accommodated on the Dauki Fault is up to 3 times faster than the average rate in the past 10 Ma [*Vernant et al.*, 2014]. The surface uplift of the Shillong Plateau has occurred in the Pliocene between 3–4 Ma [*Biswas et al.*, 2007] and 3.5–2 Ma [*Najman et al.*, 2016], thereby disturbing Indian Summer Monsoon (ISM) precipitations migrating northward from the Bay of Bengal by orographically condensing portion of these moisture-bearing winds along its southern flank [*Bookhagen and Burbank*, 2010]. Over the last 8 to 6 Ma, spatial and temporal variations in exhumation and erosion rates were documented in the Bhutan Himalaya [*Coutand et al.*, 2014; *Grujic et al.*, 2006; *McQuarrie and Ehlers*, 2015]. *Grujic et al.* [2006] proposed that these variations were the result of climatic changes in the lee of the Shillong Plateau, a hypothesis later modulated by *Adams et al.* [2015], *Biswas et al.* [2007], and *Coutand et al.* [2014] who proposed instead that most of the variations reflected increased contractional strain partitioning into the Shillong Plateau. As of now, it remains debatable as to whether tectonic or climatic processes related to the formation of the Shillong Plateau have had the most measurable impact on the upper crustal exhumation of the Bhutan Himalaya.

To address this question, this study takes advantage of a strategically located foreland basin sedimentary section exposed along the Dungsam Chu near the town of Samdrup Jongkhar at the front of the eastern Bhutan Himalaya (26.8°N, 91.5°E) (Figures 1 and 2). To decipher the sedimentary record through time, we have performed geochronological (magnetostratigraphy constrained by vitrinite reflectance data and detrital apatite fission track dating), sedimentological, and palynological analyses on this 2200 m thick continuous stratigraphic section of the Siwalik Group deposits. We provide new evidences supporting an increasing strain partitioning of the India-Eurasia convergence into the Shillong Plateau since the latest Miocene.

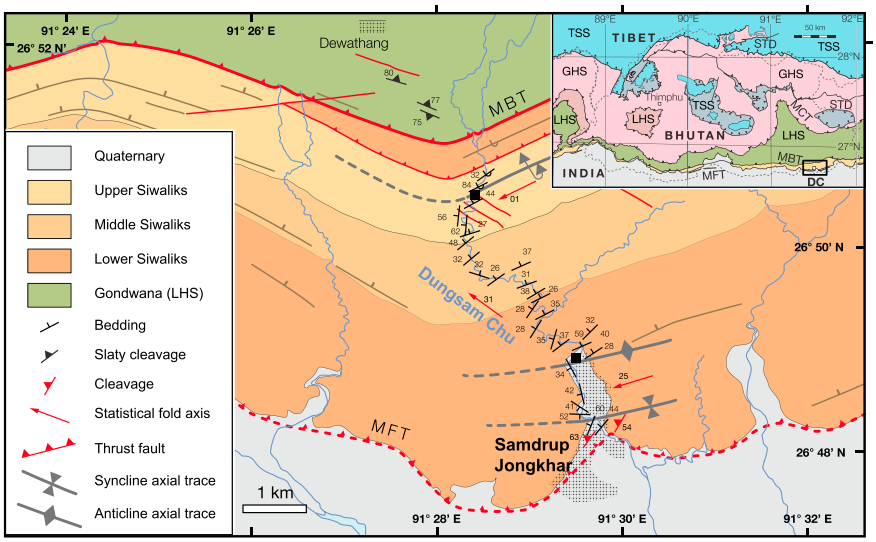

Figure 2. Geological map of the Siwalik Group around the Dungsam Chu (for location, see black frame labeled DC on the geological map of Bhutan in inset and red frame in Figure 1). Abbreviations are TSS: Tethyan Sedimentary Sequence, STD: South Tibetan Detachment, GHS: Greater Himalayan Sequence, LHS: Lesser Himalayan Sequence, MBT: Main Boundary Thrust, and MFT: Main Frontal Thrust. The Dungsam Chu section presented in this study stretches from the anticline axial plane trace to the south (26.807567°N, 91.502100°E) to the overturned syncline axial plane trace to the north (26.834967°N, 91.483617°E) (black squares).

2. Geological Setting

The Dungsam Chu section located in the foothills of the Himalaya in eastern Bhutan (Figures 1 and 2) is composed of synorogenic Neogene-Quaternary foreland sediments of the Siwalik Group forming a 2216 m thick section with a continuous exposure on freshly eroded stream banks. The section belongs to the modern Himalayan foreland fold-and-thrust belt as defined by *Hirschmiller et al.* [2014] and is bounded to the north by the Main Boundary Thrust (MBT), along which the Lesser Himalayan Sequence (LHS) has been thrust over the Siwalik Group since the late Miocene (10–12 Ma) [*Coutand et al.*, 2014], and to the south by the Main Frontal Thrust (MFT), which juxtaposes the Siwalik Group strata against the modern Ganges-Brahmaputra plain alluvial sediments (Figures 1 and 2) [e.g., *Burgess et al.*, 2012, and references therein]. Based on detrital thermochronology and/or the presence of growth strata, ongoing displacement on the MFT is suggested to have started ~2 Ma ago in central and western Nepal [*Mugnier et al.*, 2004; *van der Beek et al.*, 2006] and ~1 Ma ago in Arunachal Pradesh [*Chirouze et al.*, 2013], while the timing remains undetermined in Bhutan.

The three lithostratigraphic subgroups of the lower, middle, and upper Siwaliks crop out along the Dungsam Chu section. All along the Himalayan range, the recognition of these subgroups is based on textural differences, specifically on the proportion of different grain sizes (for a definition, see *Auden* [1935], *Gautam and Rösler* [1999], and *Quade et al.* [1995]). Typically, the coarsest sediments of the lower, middle, and upper Siwalik subgroups correspond to thin-bedded fine- to medium-grained sandstones, thick-bedded medium- to coarse-grained sandstones, and thin- to thick-bedded conglomerates, respectively. Accordingly, along the Dungsam Chu section, the boundary between the lower and middle Siwalik subgroups occurs at the first occurrence of few meters thick coarse-grained sandstone packages upsection, while the transition between the middle and upper Siwalik subgroups is where conglomeratic layers first appear [*Bhargava*, 1995; *Gansser*, 1983] (Figure 2).

3. Dating of the Dungsam Chu Sedimentary Section

To constrain the age of the Siwalik Group deposits in eastern Bhutan, we have dated the Dungsam Chu section using magnetostratigraphy constrained by vitrinite reflectance data combined with detrital apatite fission track (DAFT) dating (Figure 3).

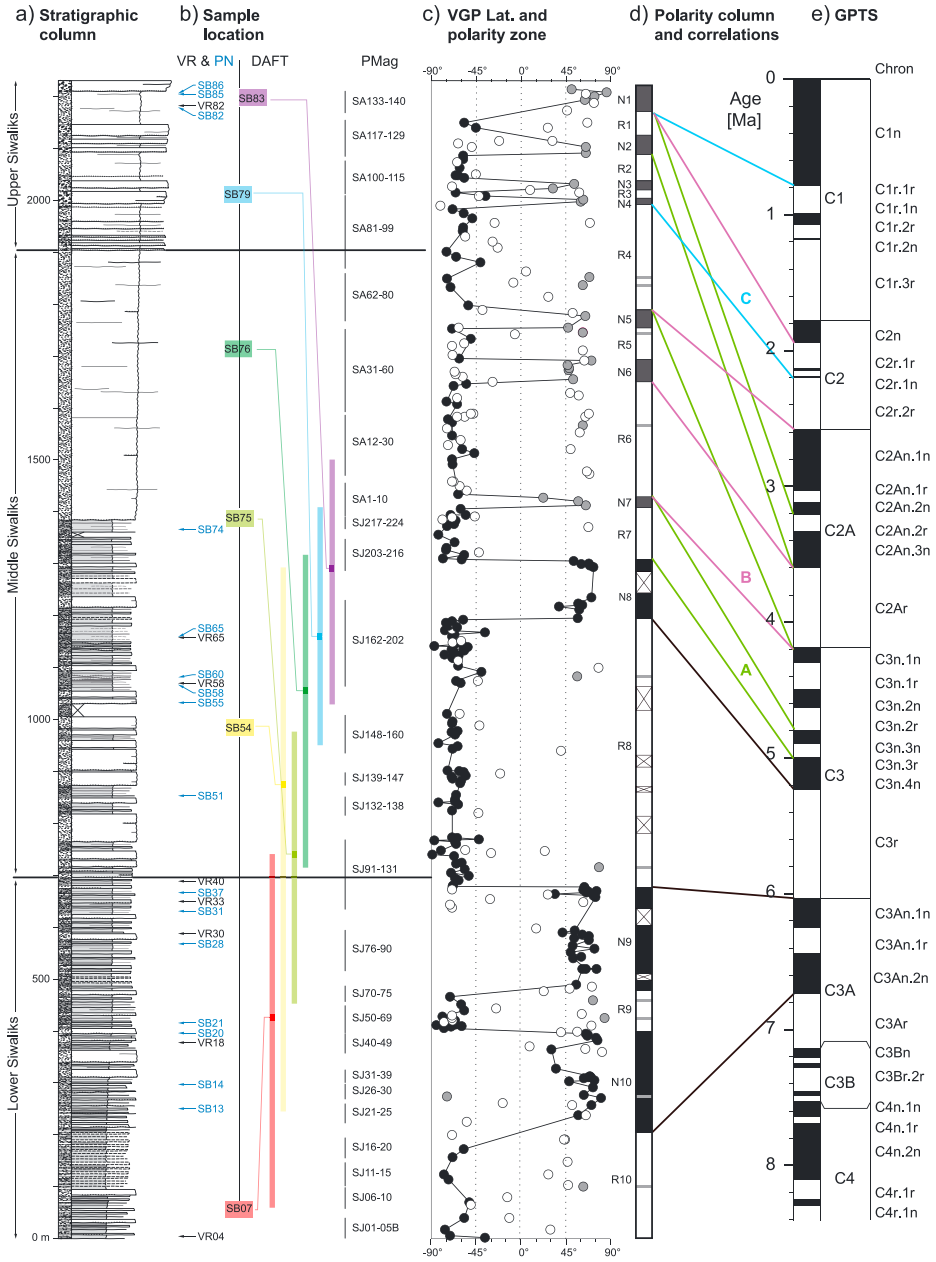

Figure 3. Sample location and magnetostratigraphy results of the Dungsam Chu section. (a) Simplified stratigraphic column (for details, see Figure 10). The horizontal scale labels C, s, S, p, c, and B are abbreviations for clay, silt, sand, pebbles, cobbles, and boulders. (b) Locations of vitrinite reflectance (VR), palynology (PN), detrital apatite fission track (DAFT), and magnetostratigraphy (PMag) samples. Maximum depositional ages deduced from DAFT are indicated by the DAFT P_1 age (solid color square) and the associated 1σ errors (light colored bars). (c) Virtual geomagnetic poles (VGP latitude) are indicated by black dots for reliable Q1 and Q2 ChRM directions, open circles depict unreliable Q3 and Q4 directions, and grey dots indicate unreliable isolated polarity directions in the lower part (below 1400 m level) and normal polarity directions in the upper part (above 1400 m level) that are unreliable due to potential normal overprints (see text). (d) Polarity column defined from our magnetostratigraphic measurements where black and white intervals indicate normal (N) and reverse (R) polarity zones, respectively. Grey intervals represent poorly constrained polarities defined either by only one or by potentially biased normal overprints in the upper part (above 1400 m level). Intervals with a cross indicate gaps in the sampling. (e) Proposed correlations of the polarity column to the geomagnetic polarity timescale (GPTS) of *Gradstein and Ogg* [2012]. Black solid lines indicate the robust correlation of the lower part based on the combination of DAFT and reliable paleomagnetic data. Green, purple, and light blue solid lines indicate uncertain correlations A, B, and C, respectively, for the upper part of the record based on DAFT and paleomagnetic data potentially biased by normal overprints. GPTS created using TSCreator v. 6.4 software from https://engineering.purdue.edu/Stratigraphy/tscreator/index/index.php based on timescale of *Gradstein and Ogg* [2012].

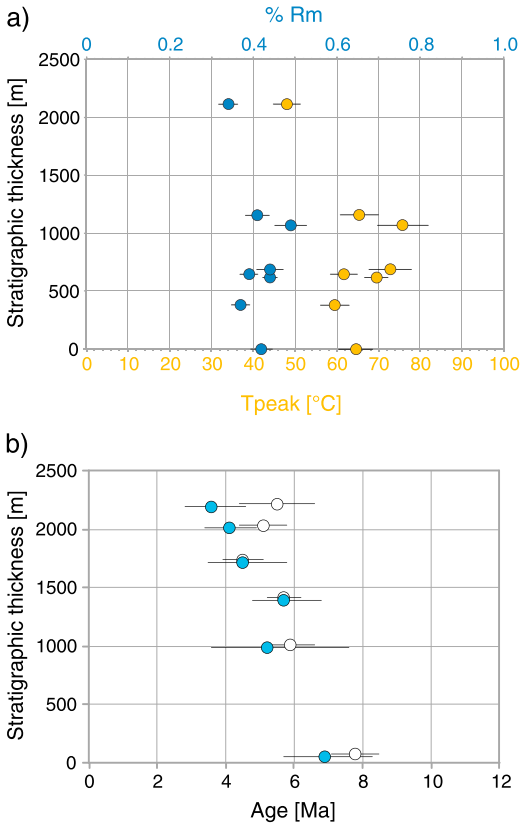

Figure 4. (a) Vitrinite reflectance data plotted against stratigraphic depth. In blue are the R_m % and in orange are the peak temperatures calculated according to the calibration of the R_m by *Barker and Pawlewicz* [1994]. (b) Detrital apatite fission track mean central ages (white circles) and P_1 ages (blue circles) plotted as a function of stratigraphic thickness from the bottom (0 m) to the top (2,216 m) of the section.

3.1. Peak Temperatures From Vitrinite Reflectance

Vitrinite reflectance analysis is used to quantify the heating of the sediments during burial and, in this study, helped to select the thermochronometer most appropriate to constrain the depositional ages of the sedimentary series. Sampling strategy and analytical procedure are provided in Text S1 in the supporting information [*American Society for Testing and Materials*, 2010; *Barker and Pawlewicz*, 1994]. The samples collected for the vitrinite reflectance analysis are composed of large coaly or banded coal particles with almost no mineral matter. They are entirely made of vitrinite, mostly derived from woody tissues, with almost no other macerals such as organic constituents derived from other nonwoody tissue like spores, pollen, resin, or other oxidized constituents (i.e., fusinites) [*International Committee for Coal and Organic Petrology*, 2001]. All the samples yielded values below 0.5% R_m, in the upper to lower range of lignite (Figure 4a and Figure S1 in Appendix A). The peak temperatures of the stratigraphically lower seven samples range between 59.5 ± 3.5 and 75.8 ± 6.1°C, without a distinguishable trend upsection, yielding a mean burial temperature of 67.1 ± 5.5°C for the lower part of the section (Figure 4a).

This lack of temperature gradient with increasing depth may be attributed to different factors:

1. The samples were collected along a northward tilted section; hence, upsection, the samples migrate along the depositional profile toward thicker portions of the Siwalik sedimentary wedge. Equivalent spatial trend of burial temperatures was observed in the North Alpine Foreland basin [*Mazurek et al*., 2006].
2. Basin modeling there [e.g., *Mazurek et al*., 2006] indicates that geothermal gradients can substantially deviate from linearity due to the lower thermal conductivity of weakly consolidated sediments at the surface as compared with the underlying basement rocks.
3. Rapid cycles of burial and exhumation of Siwalik sediments have likely prevented thermal equilibration at the scale of the basin (see example of the intramontane Angastaco Basin in NW Argentina [*Coutand et al*., 2006]). In this type of young (<15 Ma) dynamic orogenic sedimentary basins, thermal states are transient and rapidly vary along and across strike implying that our observations are hardly comparable with similar data collected >100 km east in Arunachal Pradesh by *Chirouze et al*. [2013] and several hundreds of kilometers west in central Nepal by *Mugnier et al*. [1995].

Thus, the maximum burial T_{peak} at the base of the section is significantly lower than the closure temperature of ~120 ± 20°C apatite fission track thermochronometry, excluding full thermal resetting of this radiometric system. Furthermore, the mean burial temperature of the basal sediments (67.1 ± 5.5°C) is in the range of the lowermost thermal levels of the apatite fission track partial annealing zone (for details, see Text S2 in the supporting information), suggesting that minimal to no partial resetting of the thermochronometric system

occurred after deposition of the base of the section and hence mostly preserved the thermochronometric signal from the source area.

3.2. Detrital Apatite Fission Track (DAFT) Thermochronometry

Vitrinite reflectance results yielded maximum burial temperatures that suggest that DAFT thermochonometry is likely to yield unreset cooling ages representing a maximum depositional age of the strata from which the detrital sample is derived. For details on DAFT method and sampling, see Appendix B in SI [*Brandon*, 1992, 1996, 2002; *Coutand et al*., 2014; *Donelick et al*., 2005; *Galbraith and Green*, 1990; *Reiners and Brandon*, 2006; *Vermeesch*, 2012].

The central age of the basal samples is the oldest at 7.8 ± 0.7 Ma (sample SB07) (Table 1 and Figure 4b; raw data are available in Table S1). From sample SB54 up to sample SB83 at the top of the section, the central ages are younger and vary from 4.5 ± 0.6 Ma to 5.9 ± 0.7 Ma but remain identical within error (Figure 4b). Three out of the seven samples fail the χ^2 test [*Galbraith*, 2005] with $P(\chi^2) < 5\%$ (Table 1), indicating that dispersion in the fission track grain-age distributions may be significant. Apatite fission track samples collected from bedrock samples across the modern landscape in eastern Bhutan vary significantly in a north-south direction [*Coutand et al*., 2014]. Therefore, the age dispersion observed in the detrital data along the Dungsam Chu section may be attributed to different provenance areas characterized by different exhumation rates in the upstream catchments.

Altogether, vitrinite reflectance and DAFT data clearly indicate that no partial resetting occurred along the section. In fact, the bottommost sample yields maximum burial temperatures of 65 ± 4°C and the temperature of the uppermost levels of the apatite fission track partial annealing zone is comprised between 75 and 60°C for holding time of 1 to 10 Ma, respectively [e.g., *Reiners and Brandon*, 2006]. Moreover, central DAFT ages decrease upsection (Figures 3 and 4b and Table 1), while the opposite would be expected if the samples had been reset in the sedimentary basin and subsequently re-exhumed.

To better constrain the stratigraphic age of the section, we have extracted the youngest component of the detrital age signal by decomposing the fission track grain-age distribution into peaks using the *Binomfit* software [*Brandon*, 1992, 1996, 2002] (Table 1). The three samples failing the χ^2 test (samples SB54, 79, and 83) and the basal sample SB07 yield two peaks. The older peak (P_2) represents a minor component of about 10% of the total detrital fraction for most of the samples and up to 30% for sample SB83 at the top of the section (Table 1). The younger peak (P_1) represents the mode of AFT age derived from the fastest-eroding parts of the source catchment. The fact that P_1 gets younger upsection (Figure 4b), and that there is a marked dispersion of single-grain ages, supports vitrinite reflectance results suggesting that burial heating has little or not reset AFT single-grain ages after deposition. Therefore, we use P_1 as a proxy for the maximum depositional age of the Siwalik Group along the Dungsam Chu sedimentary section. This implies that the sediments cannot be older than 6.9–1.2/+1.4 Ma at the bottom of the section (sample SB07) and 3.6–0.8/+1.0 Ma at the top (sample SB83) (Table 1 and Figure 4b). Our results are supported by unpublished detrital zircon (U-Th)/He data collected from a sample located a few meters underneath our basal sample, yielding discordant single-grain ages with a younger cluster at 7 Ma (N. McQuarrie, personal communication, 2016).

3.3. Paleomagnetic Analysis

To date the sedimentary section, we undertook a magnetostratigraphic study constrained by vitrinite reflectance and DAFT data. For details on sampling and analytical procedure, see Text S3 in the supporting information.

3.3.1. Magnetization Characteristics

Initial Natural Remanent Magnetization (NRM) intensities vary between 10^{-5} and 10^{-1} A/m and generally increase upsection, suggesting an increasing concentration of strongly magnetic iron oxides such a magnetite. Throughout the section, we observed various thermal demagnetization behaviors from which Characteristic Remanent Magnetization (ChRM) components were defined and plotted on vector end point diagrams and stereographic projections (Figure 5). Two different thermal demagnetisation behaviors related to lithological changes characterize the lower (below 1400 m) and the upper (above 1400 m) parts of the sedimentary section.

Table 1. Detrital Apatite Fission Track Results[a]

Sample	Number of Grains	Cumulative Stratigraphic Thickness (m)	Spontaneous Track Density ($\rho_s \times 10^6$ cm^{-2}) (N_s)	Induced Track Density ($\rho_i \times 10^6$ cm^{-2}) (N_i)	Dosimeter Track Density ($\rho_d \times 10^6$ cm^{-2}) (N_d)	$P(\chi^2)$ (%)	Central Age $\pm 1\sigma$ (Ma)	U (ppm)	P_1 (Ma)	P_1 95%CI (%)	P_2 (Ma)	P_2 95%CI (%)
SB07	23	50	0.1383 (194)	4.6433 (6,513)	1.4585 (5,090)	38.8	7.8 ± 0.7	42	6.9–1.2/+1.4	88.8	12.2–3.3/+4.5	11.2
SB54	26	985	0.0978 (183)	4.7313 (8,850)	1.4889 (5,090)	1.7	5.9 ± 0.7	42	5.2–1.6/+2.4	86.2	10.0–8.0/+39.5	13.8
SB75	21	1390	0.0830 (126)	4.0221 (6,104)	1.4865 (5,291)	18.8	5.7 ± 0.5	36	5.7–0.9/+1.1	100	x	x
SB76	14	1715	0.0635 (59)	3.8566 (3,581)	1.4882 (5,291)	51.5	4.5 ± 0.6	44	4.5–1.0/+1.3	100	x	x
SB79	24	2010	0.1098 (195)	5.6400 (10,018)	1.4899 (5,291)	0.0	5.1 ± 0.7	50	4.1–0.7/+0.8	90.4	12.7–2.9/+3.8	9.6
SB83	17	2193	0.1227 (137)	6.2963 (7,028)	1.4916 (5,291)	0.0	5.5 ± 1.1	62	3.6–0.8/+1.0	69.5	15.2–4.5/+6.3	30.5

[a] Abbreviations are N, number of individual grains dated per sample; ρ_s, spontaneous track density; ρ_i, induced track density; N_s, number of spontaneous tracks counted; N_i, number of induced tracks counted; ρ_d, induced track density in external detector adjacent to dosimetry glass; N_d, number of tracks counted in determining ρ_d; $P(\chi^2)$, χ^2 probability. Apatite aliquots were mounted in araldite epoxy on glass slides, ground and polished to expose internal grain surfaces, then etched for 20 s in 5.5 M HNO_3 at 21°C to reveal spontaneous fission tracks. All mounts were prepared using the external detector method [*Hurford and Green*, 1983]. Samples and CN5 glass standards were irradiated with thermal neutrons in the Oregon State University reactor. After the irradiation, the low-U muscovite detectors that covered apatite grain mounts and glass dosimeter were etched in 40% HF for 45 min at 21°C to reveal induced fission tracks. Samples were then analyzed using a Kinetek computer-controlled stage driven by the FTStage software [*Dumitru*, 1993] attached to a Zeiss Axioplan microscope. Dry counting was done at a magnification of ×1000, and fission track ages were calculated using a weighted mean Zeta calibration factor based on International Union of Geological Sciences ages standards [*Hurford*, 1990; *Miller et al.*, 1985]. Based on 23 analyses, the Zeta the ζ for the operator (I. Coutand) is 370.6 ± 5.0.

In the lower part composed of the lower and middle Siwalik subgroups where the samples are fine grained, (paleomagnetic samples SJ1-SJ224; for sample location, see Figure 3), demagnetizations were mostly complete below 400°C (Figures 5a and 5c). A viscous low-temperature component was often removed below 150°C, while a low-temperature component (LTC) of normal polarity generally demagnetized between 130 and 300°C and was interpreted as an overprint. A medium-temperature component (MTC) was also typically demagnetized between 130 and 400°C and often overlapped with the LTC along great circle paths on stereographic projections (Figure 5d). This MTC displays either normal or reversed polarity directions and was interpreted as representing the ChRM in the lower and middle Siwalik subgroups. Above 300°C, an increase in both remanence intensity and susceptibility is characteristic of the transformation of iron sulphides into magnetite upon heating. This suggests that iron sulphides, such as greigite, may be carrying the ChRM in the rocks of the Siwalik Group as it was observed elsewhere in the eastern Himalaya [*Chirouze et al.*, 2012].

The upper part of the section, composed of the middle and upper Siwalik subgroups, is characterized by an abrupt increase of the sample grain size from fine- to dominantly medium-grained sandstones (paleomagnetic samples SA1-SA140; for sample location, see Figure 3). These samples yielded generally higher initial NRM intensities but more erratic unstable thermal demagnetization paths such that many samples did not yield interpretable directions (Figures 5e and 5f). This is attributed to the larger grain size yielding multidomain magnetic grains [*Butler*, 1992]. The samples that did yield interpretable demagnetization paths had much higher unblocking temperatures ranging from 300 to 600°C and sometimes extending up to 680°C. This behavior is typical of a remanence dominated by magnetite-like minerals and the occasional occurrence of hematite.

3.3.2. ChRM Direction Analyses

ChRM directions were calculated using a minimum of four consecutive heating steps usually decreasing toward the origin such that line fits were generally not anchored to the origin. Some demagnetization paths showing a steady direction but no significant decrease in intensity upon demagnetization were forced through the

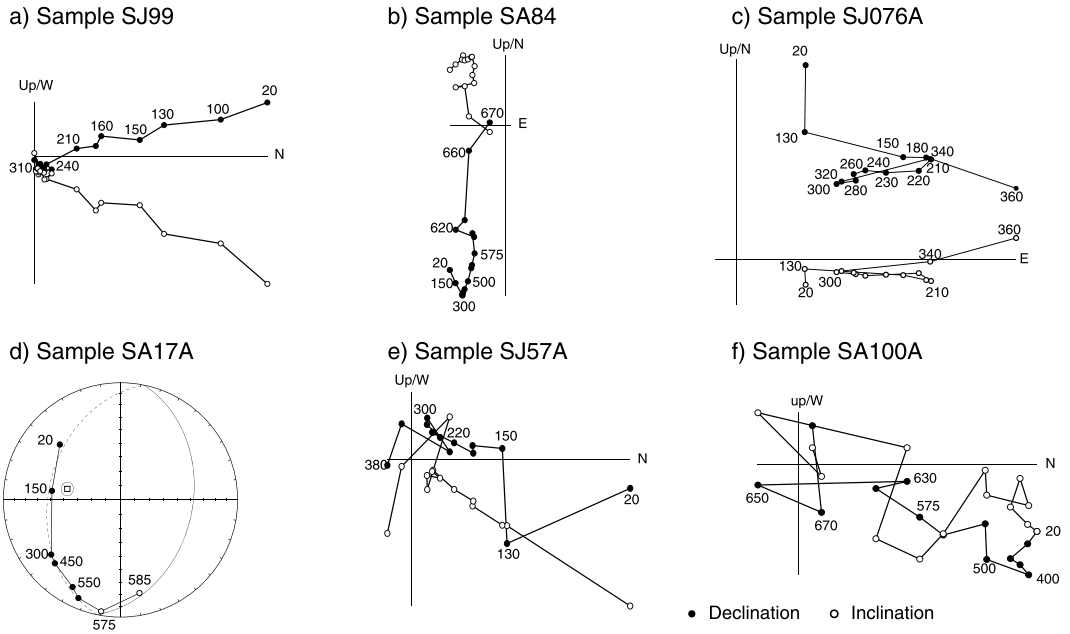

Figure 5. Representative thermal demagnetization diagrams. Full and open symbols are projections on the horizontal and vertical planes, respectively. The numbers next to the symbols indicate the temperature of demagnetization step in °C. (a and b) Reliable direction and polarity from group Q1. (c and d) Reliable polarity but unreliable direction from group Q2. Figure 5d is a typical demagnetization path on which great circle analysis was performed on stereographic projection [*McFadden and McElhinny*, 1988]. (e and f) Unreliable direction and polarity from group Q3. Samples SJ are from the lower part of the section, while samples SA are from the upper part of the section.

origin (Figure 5; data are provided in Table S2 in Appendix C). Line fits with a Maximum Angular Deviation (MAD) above 30° were systematically rejected. Because of the common occurrence of secondary overprints with normal polarities, sometimes persisting at relatively high demagnetization temperatures, a careful selection of ChRM directions was performed by ordering them into four quality groups (Table S2). In the Quality 1 (Q1) group are the ChRM directions of normal or reversed polarity from which a well-defined direction was determined from stable and linear demagnetization paths, yielding MAD typically below 15° (Figures 5a and 5b). In the Quality 2 (Q2) group, normal or reversed polarities are clearly defined but the directions are less reliable because of directional scatter and/or overlapping secondary overprint (Figures 5c and 5d). The polarity determination of Quality 3 (Q3) remains ambiguous due to the weakness of the signal and/or strong overlapping with the normal secondary polarity (Figures 5e and 5f). This group also includes poorly indurated samples that were destroyed before we could process enough measurements to extract reliable ChRM directions. The Quality 4 (Q4) group includes data displaying outlying directions that were rejected following an iterative cutoff protocol described in the paragraph below.

The reversed polarity directions were more reliably identified than normal ones because the latter may have resulted from a full overprint of an originally reversed direction. The distinction between a primary component and a normal secondary overprint was also aided by the fact that the primary directions have been affected by significant counterclockwise rotations about vertical axes (Figure 6). Great circle analysis [*McFadden and McElhinny*, 1988] was applied to some Q2 and Q3 samples, when the contribution of the direction of the secondary normal polarity overlapped a reversed polarity direction carried by only a few points. For this procedure the mean of the Q1 reverse polarity directions was used as set point, and the procedure described by [*McFadden and McElhinny*, 1988] was used to extract the primary direction from the great circle analysis (Figure 6). To remove greatly outlying and transitional directions, an iterative cutoff was applied to the virtual geomagnetic poles (VGPs) derived from the obtained ChRM Q1 and Q2 directions. VGP directions lying more than 45° from the mean VGP were iteratively cut off and rejected in the Q4 quality group. This procedure was performed on normal and reversed polarity data sets separately. The remaining Q1 and Q2 ChRM directions cluster in antipodal fashion after tilt correction, suggesting a primary origin of normal and reversed polarities (Figure 7).

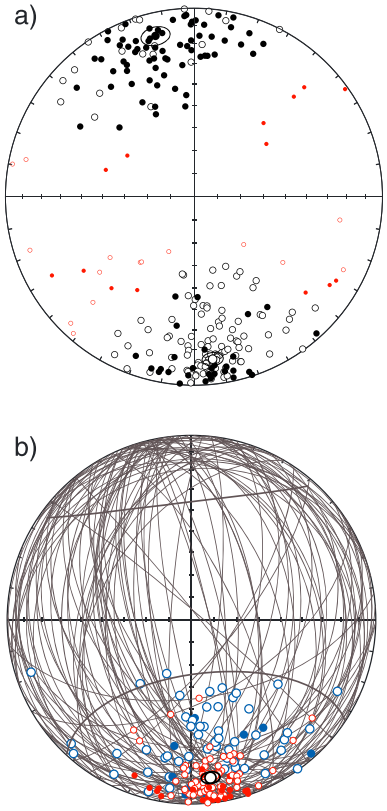

Figure 6. (a) Stereographic projections of Q1 and Q2 ChRM directions projected on the lower (filled symbols) and upper (open symbols) hemispheres. Directions reported in red have VGP over 45° from the mean VGP and were iteratively cut off. (b) Great circle analysis. The set point (black dot) is defined by the mean of Q1 directions (blue dots). Obtained reversed directions (red points) are defined by the point on each great circle that is nearest to the set point. Filled (open) symbols are projections on the lower (upper) hemisphere.

The section being monoclinally tilted, a fold test was not applicable. The reversals test [*Tauxe*, 1998], applied to Q1 and Q2 ChRM directions, was negative after flipping reversed directions to antipodal normal orientations. The negative reversals test is expected with data including partially overprinted directions obtained from great circle analysis, but it does not affect the validity of the reversed polarity determinations.

The resulting set of 220 Q1 and Q2 ChRM directions provides paleomagnetic polarity determination at an average interval of 10 m throughout the stratigraphic section with several larger gaps due to a lack of outcrop or the inadequacy of rock type (usually weathered coarse-grained sandstones) that yielded noninterpretable demagnetization paths (Figure 3). Reversed polarity directions were unequivocally recognized, but normal polarity directions have been determined more cautiously with regard to possible secondary normal overprints. In the lower part of the section, normal polarities are well expressed in linear demagnetization paths and systematically observed in consecutive intervals yielding credit to these normal polarity zones. In addition, normal overprints observed in reversed polarity samples of the lower part usually do not persist above 300°C such that higher-temperature normal directions can be confidently identified. In the upper part of the section, however, normal polarity directions are often unstable, not systematically consecutive, and normal overprints of reversed direction are found in high-temperature ranges suggesting that some samples have been fully remagnetized.

3.3.3. Magnetostratigraphy: *C* Correlation to the Geomagnetic Paleomagnetic Polarity Timescale

Because the dating from biostratigraphy or volcanic ash layers is not possible, our magnetostratigaphic study relies on detrital apatite fission track analysis to provide independent constraints for the correlation of our paleomagnetic results with the geomagnetic polarity timescale (GPTS) of *Gradstein* [2012]. Several layers in the section are thus assigned a maximum depositional age based on unreset DAFT ages from the sedimentary series (Figures 3b and 3d and Table 1). Polarity zones are defined by at least two consecutive paleomagnetic sites bearing the same polarity such that isolated points were discarded from the definition of polarity zones. Twenty polarity zones including 10 normal (N1 to N10) and 10 reversed (R1 to R10) were identified in the section (Figure 3). Because normal overprinting commonly occurs in the coarser-grained top part of the section, the normal zones (N2, N3, N4, and N5) are considered less reliable and have been given less weight in the following correlations.

3.3.3.1. Correlation of the Lower Part of the Section

DAFT data suggest that the stratigraphic age at the bottom of the section is younger than 6.9–1.2/+1.4 Ma (Table 1). As a starting point for our correlations, we used the longest observed reversed polarity interval R8 yielding the most reliable result below the 1400 m level within fine-grained facies in the lower to middle

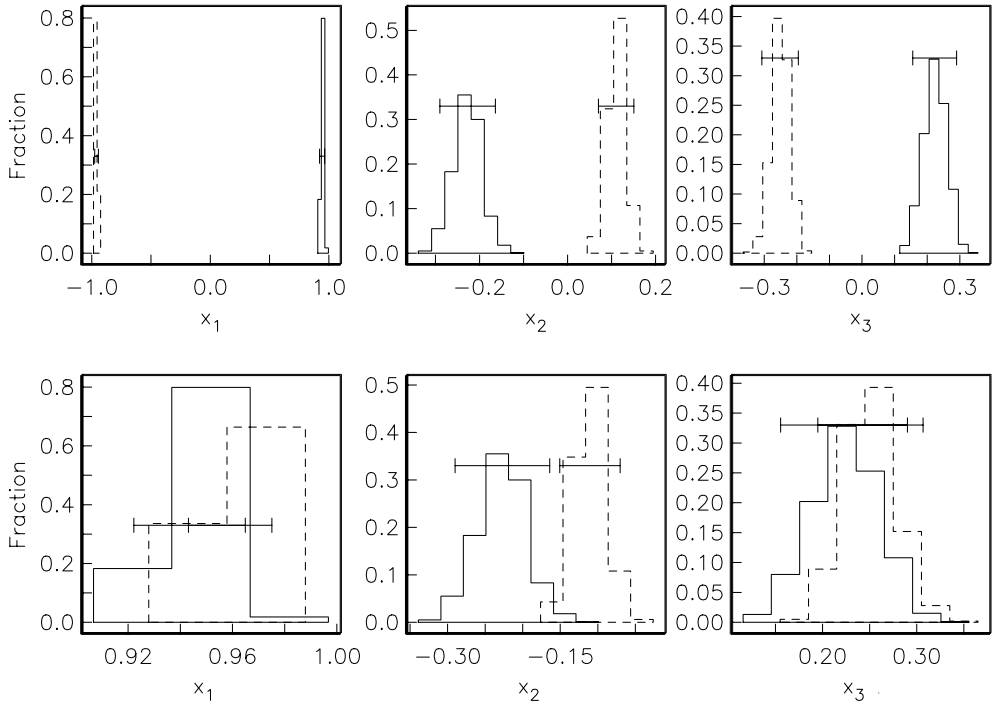

Figure 7. The reversals test [*Tauxe*, 1998] applied to Q1 and Q2 ChRM directions is negative as shown in this figure. In this test normal and reversed directions are compared in X, *Y*, *Z* coordinates (top row) before and (bottom row) after flipping reversed directions into normal coordinates. The test is positive if these directions are indistinguishable at 95% level of confidence such that their 95% confidence interval overlaps on bottom diagrams. In *XYZ* coordinates, 95% confidence intervals of average normal and reverse directions are statistically different as shown in the figure.

Siwalik subgroups. In the age range allowed by DAFT data, there are three possible correlations of the long reversed interval R8: (a) a combination of C3Br.2r to C3A (starting at 7.454 and ending at 6.733 Ma, respectively), (b) C3r (6.033–5.235 Ma), or (c) C2Ar (4.187–3.596 Ma) (Figures 3d and 3e). Correlating R8 with C2Ar is easily rejected because the short N8, N7, and N6 overlying R8 likely do not represent the relatively long dominantly normal interval C2A. Correlating R8 to C3Br.2r and C3Ar implies that the two normal chrons within C3B have been missed, while below R8, the dominantly normal polarity zones N9 to N10 provide a good counterpart to C4n chrons. However, above R8, the relatively short N8 and N7 do not provide a good fit to the relatively long normal chrons of C3A without involving substantial variations in sediment accumulation rate. Finally, correlating R8 with C3r provides the best fit without chron omission and significant accumulation rate variations. Below R8, N9 and N10 can be easily linked to C3An.1n and C3An.2n, respectively, while above, N8 fits well with Cn3.4n. This correlation places the base of our stratigraphic section at $<$7 Ma and the lower to middle Siwalik subgroups boundary at ~6 Ma. This is our preferred correlation for the basal part of the Dungsam Chu section.

3.3.3.2. Correlation of the Upper Part of the Section

The upper part of the section comprises coarser-grained lithologies and is more challenging to interpret. It is bracketed at the bottom by R8 that we preferentially correlate with C3r and constrained by a maximum depositional age of 3.6–0.8/+1.0 Ma by DAFT data at the top. Under these conditions, we hereafter investigate the possibilities of correlating the most reliable long reversed zones R6 and R4 to the longest reversed chrons C2Ar, C2r, or C1r.3r (Figure 3).

3.3.3.2.1. Correlation A

Correlation A relies on correlating R4 with C2Ar (start at 4.187 Ma) and R6 to C3n.2r (start at 4.799 Ma). In this case, each normal polarity zone between R4 and R8 has a matching chron within the GPTS without omission. R5, R6, and R7 correlate with C3n.1r, C3n.2r, and C3n.3r (starting at 4.493, 4.799 and 4.997 Ma), respectively. The normal zones N5, N6, N7, and N8 are consequently correlated with C3n.1n to C3n.4n (starting between 4.300 and 5.235 Ma). This correlation places the middle to upper Siwalik subgroups boundary at ~4 Ma and implies that the top of the section is about 3 Ma in age.

Table 2. List of Magnetostratigraphic Correlations, the Modeling Parameters, and the Costs of the Best Correlations[a]

Reference Ages (Ma)	Reference Chrons	Nbr Res	Maximum Path	Gap Factor	Maximum Substitution	Substitution Distance	Cost	Run Name
0–14.8	C1n-C5ADr	5,000	20,000	0	10	1	6.09	Q1
0–14.8	C1n-C5ADr	5,000	20,000	0	5	1	6.09	Q2
0–14.8	C1n-C5ADr	5,000	20,000	0	10	10	30.86	Q3
0–14.8	C1n-C5ADr	5,000	20,000	10	10	1	12,353.00	Q4
9.740–14.8	C5n.1n-C5ADr	1,000	10,000	0	10	1	6.30	Q5
9.740–14.8	C5n.1n-C5ADr	1,000	10,000	0	5	2	10.88	Q6
9.740–14.8	C5n.1n-C5ADr	1,000	10,000	0	10	10	31.91	Q7
9.740–14.8	C5n.1n-C5ADr	1,000	10,000	10	10	1	35897.30	Q8
0–8.664	C1n-C4r.2r.1n	1,000	10,000	0	10	1	5.92	Q9
0–8.664	C1n-C4r.2r.1n	1,000	10,000	0	5	2	9.76	Q10
0–8.664	C1n-C4r.2r.1n	1,000	10,000	1	10	1	14.16	Q11
0–8.664	C1n-C4r.2r.1n	1,000	10,000	0	10	10	51.17	Q12

[a]Three groups of stochastic analyses with different reference age constraints were performed. For each age group we ran four experiments with different modeling parameters (gap factor, maximum substitution, and substitution distance). For the definition of the parameters for stochastic magnetostratigraphic correlation, refer to *Lallier et al*. [2013]. The best runs are Q1, Q2, Q5, and Q9. Q5 is incompatible with DAFT data and hence was discarded; Q1, Q2, and Q9 yielded nearly identical correlations with Q9 having the lower cost. Shadings define three different groups of models covering different time periods (reported in the first column of the table labeled "age reference").

3.3.3.2.2. Correlations B and C

In correlation B, we link R6 to C2Ar (4.187–3.596 Ma), N7 to C3n.1n, and hence assume that C3n.2n and C3n.3n have been missed. Normal zones N5 and N6 fit relatively well with C2An.1n and C2An.3n chrons with a potentially missed normal zone between N5 and N6 corresponding to C2An.2n that could coincide with the isolated normal polarity point located within the R5 zone. Above N5, two correlations can be proposed. Either (B) the zones R1, R2, R3, and R4 correspond to the dominantly reversed interval C2r (ranging between 1.945 and 2.581 Ma) assuming that N2, N3, or N4 are normal overprints or (C) the zones R1, R2, R3, and R4 correspond to the reverse chrons from C1r.1r to C2r.2r (ranging between 0.781 and 2.581 Ma) assuming that N2, N3, or N4 are normal polarity zones within the corresponding chrons range. Correlations B and C place the middle to upper Siwalik subgroups boundary at 2–2.5 Ma and 1.5 Ma, respectively.

It remains difficult to discriminate between correlation A, which a priori yields a better pattern fit to the GPTS, and correlations B or C, which cannot be rejected because of the potential secondary overprints in the upper part of the section.

3.3.4. Magnetostratigraphic Correlations Using *Qupydon* Software

To quantify the ambiguities in the manual (i.e., deterministic) magnetostratigraphic correlations, we have performed stochastic modeling of the polarity column using the software Qupydon [*Lallier et al*., 2013] implementing the Dynamic Time Warping algorithm. Input data are the geomagnetic polarity timescale (GPTS) of *Gradstein and Ogg* [2012] and the thicknesses of polarity zones measured in the Dungsam Chu sedimentary section. By constraining the length of the GPTS, we have explored the above discussed correlation schemes by performing two sets of correlations (Table 2).

As a reference polarity section, we first selected the segment of the GTPS that covers all the known depositional ages of Siwaliks [e.g., *Ojha et al*., 2009], which range from chron C1n to C5ADr (0–14.775 Ma). Our polarity column contains 19 polarity zones, and the reference section of the GTPS contains 80 chrons. Accordingly, we have calculated 20,000 correlations and analyzed the 5000 best correlations determined via the best fit (or "minimum cost" [*Lallier et al*., 2013]) correlation. The numerical algorithm includes three calculation parameters: a maximum substitution, a gap factor, and a substitution distance. The maximum substitution is the maximum number of reference chrons that may be correlated to one chron of our polarity column. A gap factor equal to 0 yields a correlation with higher sedimentation rate, while a high gap factor (e.g., 10) stretches the correlation within the imposed reference timescale. A substitution distance equal to 1 allows short-term variation in sedimentation rate, while for a substitution distance >1, the software is forced to find correlations that minimize local variations of the sedimentation rates inducting gaps in the correlation [*Lallier et al*., 2013]. We set the values of those three parameters by trial and error. We set the gap factor between 10 and 0, the maximum substitution to 10, and in all our analyses, substitution distances of 1 or 2 yielded significantly lower cost correlations than a substitution distance of 10.

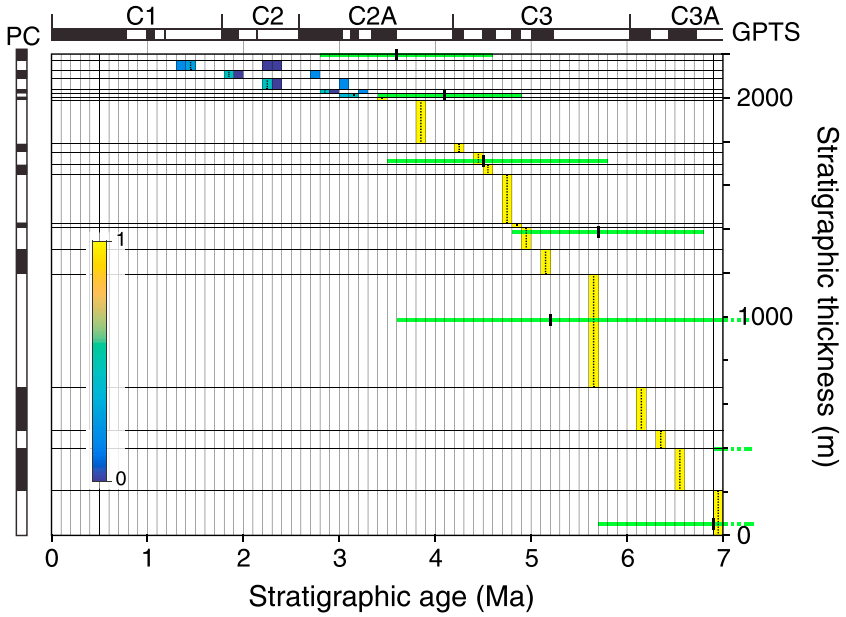

Figure 8. Weighted density age versus depth plot of the 13 best correlations for the Dungsam Chu section for the best run Q9. On the top is the GTPS chart, and on the left side is our polarity column (PC). Results with reference scale C1n-C4r.2 r (from GPTS of *Gradstein and Ogg* [2012]). Number of results = 1000, maximum paths = 10,000, gap factor = 0, maximum substitutions = 10, and substitution distance = 1. Dashed vertical lines indicate the "best solution" (cost = 5.9), also indicated in Figure 9. Horizontal green lines are the detrital apatite fission track ages. The color column to the right is the weighted density of points indicative of the goodness of fit.

When setting the age of the base of the Siwalik Group at ~14 Ma as is suggested elsewhere along the strike of the range [e.g., *Ojha et al*., 2009], statistical distribution of the 5000 best correlations yielded a large range of correlations (Table 2). However, along the Dungsam Chu section, because the DAFT analysis indicates that the base cannot be older than ~7 Ma, we have performed a second correlation using a reference scale covering chrons C1n-C4r.2r (0–8.771 Ma) (Table 2 and Figure 9). In all the analyses, we observed that the cost of correlation starts to decrease for the best 100 correlations (see related discussion by *Lallier et al*. [2013]), while the approximately 20 best correlations yield the least scatter. The best runs are Q1, Q2, Q5, and Q9 (Table 2). Q5 is incompatible with DAFT data and hence was discarded; Q1, Q2, and Q9 yielded nearly identical correlations with Q9 having the lower cost and representing the best model. For this model, we therefore further analyzed the 13 best correlations in which the 14 older polarity zones yield the same goodness of fit to the reference scale, while the top 5 zones display some scatter (Figure 8). The top of this correlation is similar to slightly younger than the manual correlation C, the top polarity zone correlating with C1r.3r (1.185–1.778 Ma) or C2r.2r (2.148–2.581 Ma), with the former having higher probability (Figure 9c). The bottom of the section correlates well with chron C3Ar (6.733–7.140 Ma).

We conclude that the stochastic correlation Q9 close to manual correlation C is the best option for the Dungsam Chu section, with an age at the base of ~7 Ma and at the top of ~1 Ma (Figure 9c).

4. Sedimentology

In addition to geochronological analyses, we have performed a sedimentological study of the Siwalik deposits to establish the nature and changes of their sedimentary environments in eastern Bhutan.

4.1. Facies Analysis

We carried out a sedimentological analysis using a standard method of facies analysis. Twelve facies were identified on the basis of their lithology, sedimentary structures, and trace fossils before being interpreted in terms of depositional processes (Table 3). Along the Dungsam Chu section, these facies co-occur in four assemblages, which were interpreted in terms of depositional environments (Table 4). Indeed, facies assemblages are more representative of depositional environments than individual facies alone, the latter rather

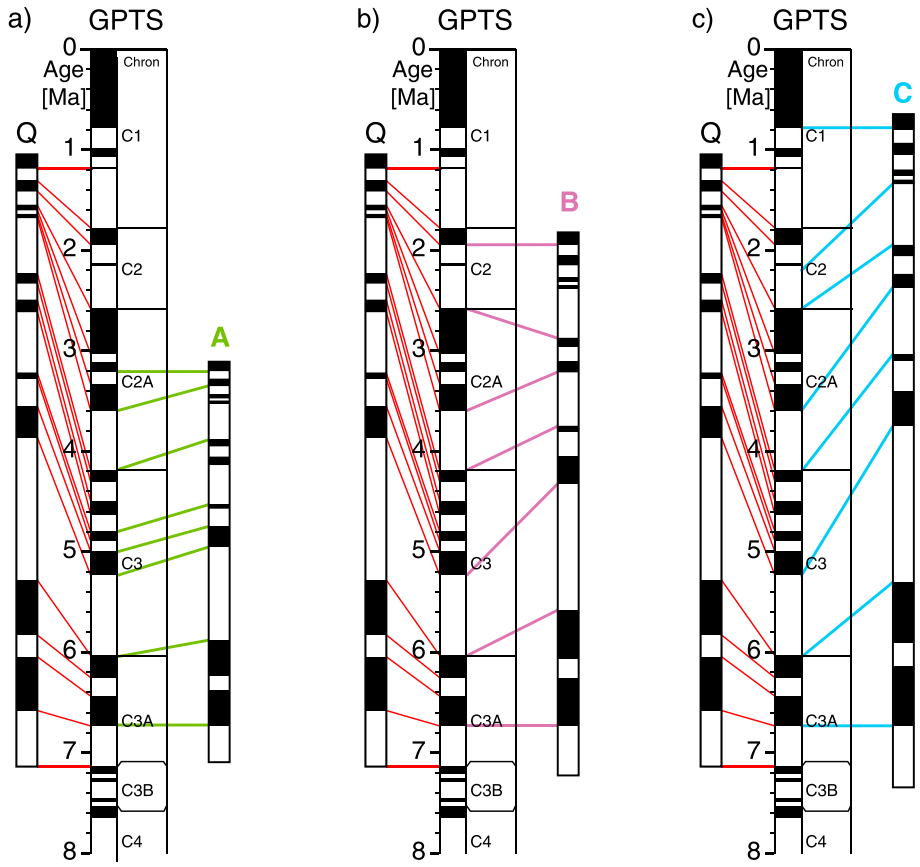

Figure 9. (a–c) Comparison of the best stochastic correlation with deterministic correlations A, B, and C. In the middle is the GTPS of *Gradstein and Ogg* [2012]. To the left is the best correlation obtained by the *Qupydon* software using the younger part of the reference scale (Q9). To the right are the manual correlations A, B, and C.

depending on the sediment nature or on elementary hydrodynamic, bioturbation, and pedogenic processes. The facies assemblages were recognized in specific locations throughout the sedimentary section and used to divide it into four units bearing different environmental characteristics. The distribution of these units was documented by a stratigraphic column constructed from outcrop observations along the Dungsam Chu transect (Figures 2 and 10). Along this transect, horizontal distances were measured using both a GPS and a decameter scale before being converted into sediment thicknesses using strike and dip measurements. Descriptions and interpretations of the four identified units in terms of depositional processes and environments are presented below, from the bottom (unit 1) to the top (unit 4) of the section.

Unit 1 comprises eight facies: one pedogenic (F1), two clayey (F2 and F3), one heterolithic (F4), and four sandy facies (F5, F8, F9, and F10) (for a detailed description, see Tables 3 and 4 and Figure 11). Among these facies, the presence of thick-bedded (centimeters to meters thick) dark grey to black claystone layers indicates subaqueous sediment fallout from suspension; massive or normally graded to flat- and cross-laminated sandstones and occasional soft-sediment deformation point to subaqueous gravity flow; flat- to cross-bedded sandstones combined with climbing and wave ripples, as well as bioturbation (among which burrows of *Planolites* and *Diplocraterion*), suggest the deposition of a sandy bed load transported by subaerial to subaqueous either confined or unconfined flow (the difference is not discernable in the field). Altogether, these deposits are interpreted as representing different parts of a river-dominated deltaic system [e.g., *Collinson*, 1969; *Hyne et al*., 1979; *Marshall*, 2000; *Tye and Coleman*, 1989]. This system may have developed in either a lacustrine or a marine environment because inferred depositional processes can occur in both settings [e.g., *Collinson*, 1969; *Hyne et al*., 1979; *Marshall*, 2000]. Moreover, the sedimentary series does not contain any macrofossil or microfossil (e.g., shells or foraminifera) that can help to discriminate the nature of the water body. At first glance, a lack of obvious marine evidence thus suggests a lacustrine delta. However,

AGU Tectonics

10.1002/2016TC004258

Table 3. Summary of the Facies Characteristics Observed in the Dungsam Chu Section and Their Interpretations in Terms of Depositional Processes

Facies Code	Facies Description	Inferred Depositional Processes	Environmental Interpretation	References
F1 (Figure 11a)	Root traces	Pedogenic processes	Paleosols	*Retallack* [1988]
F2 (Figure 11b)	Centimeters to decimeters thick, dark grey to black, silty carbonaceous shales, massive to flat laminated, with gradational to sharp basal surfaces, and frequent plant fragments	Organic-rich subaqueous suspension fallout	Interfluve or interdistributary-bay deposits	*Helland-Hansen* [2010], *Hyne et al.* [1979], and *Tye and Coleman* [1989]
F3 (Figure 11c)	A decimeter to meters thick, dark grey, silty shales to sandy siltstones, massive to flat laminated, with gradational to sharp basal surfaces, and occasional plant fragments	Subaqueous suspension fallout	Interdistributary-bay or prodelta to offshore deposits	*Helland-Hansen* [2010], *Hyne et al.* [1979], and *McCormick and Grotzinger* [1993]
F4 (Figure 11d)	Decimeters to meters thick, thin-bedded heterolithics, with gradational to sharp basal surfaces, occasional soft-sediment deformation structures, and plant fragmentsHeterolithic packages are composed of (1) millimeters to a decimeter thick, dark to light grey, clayey siltstones to fine-grained sandstones, massive or flat to undulating laminated, and (2) millimeters to a decimeter thick, light grey to yellow, fine- to coarse-grained sandstones, massive or normally graded to flat and cross laminated, with flat to irregular basal surfaces, rip-up clasts, and occasional burrows	Deposition from subaqueous gravity flows alternating with suspension fallout	Distal delta front to prodelta deposits	*Tye and Coleman* [1989], *Gani and Bhattacharya* [2007], *Helland-Hansen* [2010], and *Plink-Björklund and Steel* [2006]
F5 (Figure 11e)	Decimeters to a meter thick, light grey, medium- to coarse-grained sandstones, massive or with centimeters to a decameter thick sequences of normally gradings and flat laminations, as well as sharp to erosional basal surfaces, frequent lignite grains, and occasional burrows	Deposition from subaqueous gravity flows	Distal delta front deposits	*Gani and Bhattacharya* [2007], *Myrow et al.* [2008], and *Plink-Björklund and Steel* [2006]
F6 (Figure 11f)	Decimeters to meters thick, thick-bedded heterolithics, poorly to moderately bioturbated, with gradational to sharp basal surfaces, occasional soft-sediment deformation structures, and lignite grains Heterolithic packages are composed of (1) a centimeter to centimeters thick, dark to light grey, clayey siltstones to fine-grained sandstones, massive or flat-laminated, and (2) centimeters to decimeters thick, light grey to yellow, fine- to coarse-grained sandstones,	Deposition from combined subaqueous oscillatory and unidirectional flows alternating with suspension fallout	Distal delta front deposits	*Buatois* [2012], *Chan and Dott* [1986], *Helland-Hansen* [2010], and *McCormick and Grotzinger* [1993]

AGU Tectonics

10.1002/2016TC004258

Table 3. (continued)

Facies Code	Facies Description	Inferred Depositional Processes	Environmental Interpretation	References
	massive or wavy to flaser bedded, with sharp to erosional basal surfaces, and dark to light grey laminae of clayey siltstones to medium-grained silty sandstones, as well as frequent undulating, hummocky, and swaley laminations of wave ripples, intrabed gutter casts, and lignite grains, and numerous burrows (among which *Planolites* and *Diplocraterion*)			
F7 (Figures 11g–11k)	Decimeters to meters thick, light grey to yellow, fine- to coarse-grained sandstones, undulating laminated or wavy to flaser bedded, poorly to thoroughly bioturbated, with sharp to erosional basal surfaces, dark to light grey laminae of fine- to medium-grained silty sandstones, as well as hummocky and swaley lamination of wave ripples, intrabed gutter casts, soft-sediment deformation structures, lignite grains, and numerous burrows (among which *Planolites* and *Diplocraterion*)	Deposition from combined subaqueous oscillatory and unidirectional flows	Proximal delta front deposits	*Buatois* [2012], *Chan and Dott* [1986], *Gani and Bhattacharya* [2007], *Helland-Hansen* [2010], and *McCormick and Grotzinger* [1993]
F8 (Figure 11l)	A decimeter to decimeters thick, light grey, medium- to coarse-grained sandstones, flat laminated to cross laminated, with sharp to erosional basal surfaces, frequent climbing ripples, lignite grains, and lignite laminations, as well as occasional wave ripples and burrows	Deposition of a sandy bed load transported by subaerial to subaqueous unconfined flows	Mouth bar to proximal delta front deposits	*Buatois* [2012], *Marshall* [2000], *Plink-Björklund and Steel* [2006], and *Tye and Coleman* [1989]
F9 (Figure 11m)	Decimeters to meters thick, light grey to yellow, coarse-grained sandstones, massive or flat bedded to tabular and trough cross bedded (<1 m), with sharp to erosional basal surfaces, frequent lignite grains, lignite laminations, and soft-sediment deformation structures, as well as occasional climbing and wave ripples, rip-up clasts, and burrows	Deposition of a sandy bed load transported by subaerial to subaqueous confined or unconfined flows	Terminal distributary channel to mouth bar deposits	*Buatois* [2012], *McCormick and Grotzinger* [1993], *Olariu and Bhattacharya* [2006], *Plink-Björklund and Steel* [2006], and *Tye and Coleman* [1989]
F10 (Figure 11n)	Decimeters to tens of meters thick, light grey to yellow, coarse-grained sandstones, massive or flat bedded to tabular and trough cross bedded (<1 m), with erosional basal surfaces and meter-scale compound cross beds,	Deposition of a sandy bed load transported by subaerial stream or sheet flows	Sand bed channel or sheetflood deposits	*Buatois* [2012], *Jo et al.* [1997], *Marshall* [2000], *Miall* [1977, 1985], and *Wizevich* [1992]

Table 3. (continued)

Facies Code	Facies Description	Inferred Depositional Processes	Environmental Interpretation	References
	frequent reactivation surfaces, and lignite grains, occasional climbing ripples (units 1 and 2) or extrasize clasts (units 3 and 4), and rare soft-sediment deformation structures			
F11 (Figure 11o)	A decimeter to a meter thick, light grey to yellow, coarse-grained pebbly sandstones, massive or flat bedded to tabular and trough cross bedded (<1 m), with sharp to erosional basal surfaces, and occasional lignite clasts	Deposition of a sandy and pebbly bed load transported by subaerial stream or sheet flows	Pebbly sand bed channel or sheetflood deposits	*Jo et al.* [1997], *Miall* [1977, 1985] and *Wizevich* [1992]
F12 (Figure 11p)	A decimeter to tens of meters thick, pebble to cobble conglomerates, clast supported but sandy matrix rich, massive or tabular cross bedded, with erosional basal surfaces, and frequent winnowed gravels at the top	Deposition of a gravelly bed load transported by subaerial stream or sheet flows	Gravel bed channel or sheetflood deposits	*Jo et al.* [1997], *Miall* [1977, 1985], and *Ramos and Sopeña* [1983]

the occurrence of trace fossils of marine affinity like *Diplocraterion* and glauconite in clay composition (Grujic, personal communication, 2016), together with some mangrove to freshwater swamp pollen taxa (*Nypa* and *Neocouperipollis*; for details, see section 5), suggests an environment influenced by brackish water and indicates that a marine interpretation is viable. At its top, unit 1 grades quickly (within a few meters) into unit 2 where new facies (F6 and F7) appear, their first occurrence being dated at ~6.4 Ma.

Unit 2 comprises 10 facies: one pedogenic (F1), two clayey (F2 and F3), two heterolithic (F4 and F6), and four sandy facies (F5, F7, F8, F9, and F10) (Tables 3 and 4 and Figure 11). Facies characteristics are similar to unit 1 but additionally include massive or wavy- to flaser-bedded sandstones with undulating, hummocky, and swaley laminations of wave ripples indicating deposition or reworking by waves. These deposits represent a wave-influenced deltaic depositional system [e.g., *Chan and Dott*, 1986; *Helland-Hansen*, 2010; *McCormick and Grotzinger*, 1993; *Myrow et al*., 2008]. As for unit 1 and without clear sedimentary features, trace fossils, or fossils supporting one hypothesis or the other, this deltaic environment may have developed in either a lacustrine or a marine setting. However, the occurrences of trace fossils of marine affinity like *Diplocraterion*, of glauconite (Grujic, personal communication, 2016) and of some mangrove to freshwater swamp pollen taxa (*Nypa* and *Neocouperipollis*, together with *Pelliciera and Brownlowia*; for details, see section 5), associated with the wave-influenced facies, rather indicate that the deltaic system of unit 2 was subjected to intermittent marine influences. At the top, unit 2 sharply gives way to unit 3 at ~4.9 Ma.

Unit 3 comprises two sandy facies (F10 and F11) (Tables 3 and 4 and Figure 11). In this unit, the presence of massive or bedded sandstones with erosional basal surfaces, meter-scale compound cross beds, and scattered pebbles indicates the deposition of a sandy and pebbly bed load transported by subaerial either stream or sheet flows. These deposits are interpreted as representing a sandy alluvial environment [e.g., *Jo et al*., 1997; *Marshall*, 2000; *McCormick and Grotzinger*, 1993; *Miall*, 1977, 1985; *Wizevich*, 1992]. At its top, unit 3 shifts to unit 4 over a sharp transition dated at ~3.8 Ma.

Unit 4 comprises three facies: two sandy facies (F10 and F11) and one conglomeratic facies

Table 4. Summary of the Characteristics of the Facies Assemblages, Corresponding Units Observed in the Dungsam Chu Section, and Their Interpretations in Terms of Depositional Environments

Occurrence	Facies Assemblage	Facies Environmental Interpretation (See Table 3)	Inferred Depositional Environment	References
Unit 1	Facies F1, F2, F3, F4, F5, F8, F9, and F10, with glauconite and mangrove to freshwater swamp pollen taxa	Assemblage of offshore, prodelta, delta front, mouth bar, sand bed distributary channel or sheetflood, and interfluve or interdistributary bay deposits with minor paleosols	River-dominated deltaic environment with marine influences	*Hyne et al.* [1979], *Marshall* [2000], and *Tye and Coleman* [1989]
Unit 2	Facies F1, F2, F3, F4, F5, F6, F7, F8, F9, and F10, with frequent occurrences of oscillatory flows, *Diplocraterion*, glauconite, and mangrove to freshwater swamp pollen taxa	Assemblage of offshore, prodelta, delta front, mouth bar, sand bed distributary channel or sheetflood, and interfluve or interdistributary bay deposits with minor paleosols	Wave-influenced deltaic environment with marine influences	*Chan and Dott* [1986], *Helland-Hansen* [2010], *McCormick and Grotzinger* [1993], and *Myrow et al.* [2008]
Unit 3	Facies F10 and F11	Assemblage of sand bed channel or sheetflood deposits	Sandy alluvial environment, probably a distal braided-streamflow fan system	*Jo et al.* [1997], *Marshall* [2000], *McCormick and Grotzinger* [1993], *Miall* [1977, 1985], and *Wizevich* [1992]
Unit 4	Facies F10, F11, and F12, with mangrove to freshwater swamp pollen taxa	Assemblage of sand bed and gravel bed channel or sheetflood deposits	Gravelly alluvial environment, probably a proximal braided-streamflow fan system	*Jo et al.* [1997], *McCormick and Grotzinger* [1993], and *Miall* [1977, 1985]

(F12) (Tables 3 and 4 and Figure 11). Facies characteristics are similar to unit 3 but additionally include massive or bedded conglomerates with erosional basal surfaces suggesting the deposition of a gravelly bed load transported by subaerial either stream or sheet flows. These deposits represent a gravelly alluvial environment [e.g., *Jo et al.*, 1997; *McCormick and Grotzinger*, 1993; *Miall*, 1977, 1985]. The limited lateral extent of the studied section and its rock exposure (a few tens of meters) precludes clear determination of the channel pattern (braided or meandering) and organization (radial or not) of this alluvial system. Yet the analogy of our observations with the modern fluvial fans in the Himalayan foreland basin suggests that units 3 and 4 likely represent the distal and more proximal parts, respectively, of a braided-streamflow fan environment [*Jain and Sinha*, 2003; *Kumar et al.*, 2004; *Shukla et al.*, 2001]. In unit 4, a few pollens of mangrove to freshwater swamp taxa (*Neocouperipollis* and *Nypa*; for details, see section 5) are also found. However, in the absence of other marine criteria (sedimentary figures, trace fossils, or clays) and provided that these taxa may also occur in tidally influenced rivers and freshwater swamps relatively far inland [*Giesen et al.*, 2007; *Morley*, 1991; *Tomlinson*, 1994], this is not necessarily inconsistent with an alluvial interpretation for the associated deposits.

4.2. Sedimentation Rates

Using our preferred magnetostratigraphic correlation, we have constructed two sedimentary accumulation curves for the Dungsam Chu section. First, we have used the median value for the calculated sediment accumulation rates from *Qupydon* and the median age for each polarity zone (Figure 10c) and second, we have plotted the measured sedimentary thickness against the ages of corresponding GPTS 2012 chrons (Figures 10c and 12). The first curve provides instantaneous sedimentation rates for each chron, while the second one smooths the signal over several chrons and yields a longer-term trend in accumulation rates. In units 1 and 2, sedimentation rates range between 0.4 and 0.6 mm/yr with a peak at 0.9 mm/yr at the base of unit 2. Unit 3 displays scattered rates at the base with two peaks at 1.0 and 1.3 mm/yr and stable values of 0.3 mm/yr in the upper half portion continuing into the lower part of unit 4, decreasing to values $<$0.1 mm/yr at the top of the section. The slopes of the best fit lines for the three groups of datapoints in Figure 12 indicate a clear tendency for a slowdown of the sediment accumulation rates from ~0.63 mm/yr in units 1, 2, and base of unit 3 to ~0.3 mm/yr at the top of unit 3 and the base of unit 4 and ~0.07 mm/yr at the top of the section (see also the red curve in Figure 10c).

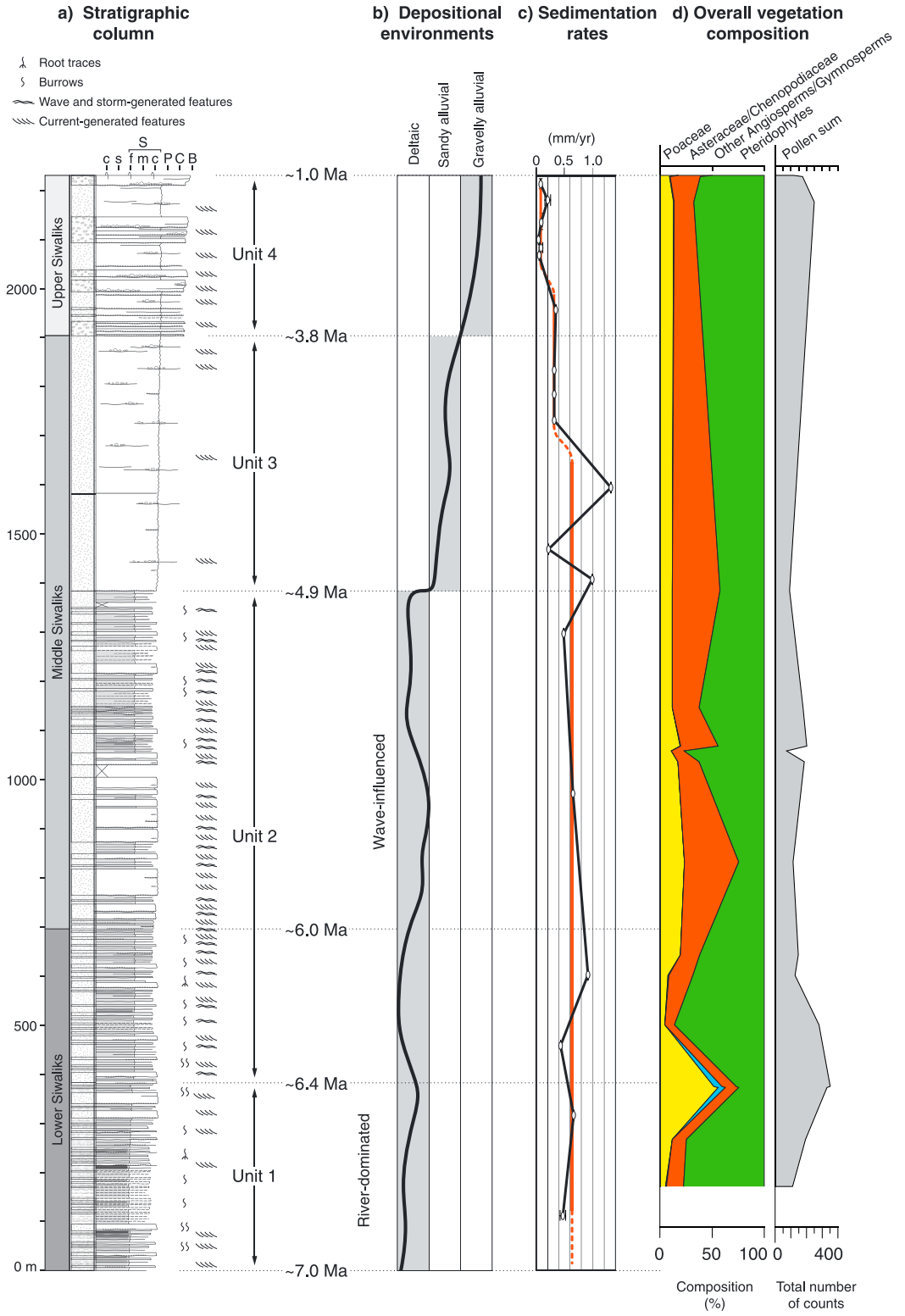

Figure 10. Measured sedimentary section of the Siwalik Group deposits exposed along the Dungsam Chu near Samdrup Jongkhar (see Figure 1 for location). (a) Stratigraphic column. The horizontal scale labels C, s, S, P, C, and B are abbreviations for clay, silt, sand, pebbles, cobbles, and boulders. Current-generated features include current-ripple laminations, tabular cross beddings, through cross beddings, and flat beddings. Wave-generated features comprise undulating and wave-ripple laminations. (b) Depositional environment evolution. (c) Sedimentation rate evolution obtained for the best correlation from *Qupydon*.

Figure 11. Photographs of outcrops depicting the most typical facies observed in the Dungsam Chu sedimentary section. (a) Facies F1 (units 1 and 2): example of a root trace. (b) Facies F2 (units 1 and 2): carbonaceous shale. (c) Facies F3 (units 1 and 2): noncarbonaceous shale. (d) Facies F4 (units 1 and 2): heterolithics with flat and undulating laminations, some rip-up clasts, and irregular surfaces of the base of the sandstone layers. (e) Facies F5 (units 1 and 2): centimeters to a decimeter thick sequences of normal gradings and flat laminations. (f) Facies 6 (unit 2): a sandstone layer of this heterolithic facies showing flaser beddings, undulating and swaley laminations, and intrabed gutter casts. Among other burrows, note the decimeter-scale *Diplocraterion* and the frequent millimeter-scale *Planolites*. (g and h) Facies 7 (unit 2): sandstone with disturbed laminations, wavy to flaser beddings, soft-sediment deformation structures, and millimeter- to centimeter-scale burrows. (i) Facies 7 (unit 2): sandstone with wavy to flaser beddings and wave ripples. (j) Facies 7 (unit 2): sandstone with flaser beddings, undulating, hummocky, and swaley laminations of wave ripples, and millimeter- to centimeter-scale burrows. (k) Facies 7 (unit 2): sandstone with disturbed laminations, soft-sediment deformation structures, and pervasive bioturbation. (l) Facies 8 (units 1 and 2): sandstone with cross laminations and climbing ripples. (m) Facies 9 (units 1 and 2): sandstone with flat and cross beds, lignite laminations, and soft-sediment deformation structures. (n) Facies 10 (units 1–4): sandstone with climbing-ripple cross-laminations, flat and cross beds, and reactivation surfaces. (o) Facies 11 (units 3 and 4): sandstone with flat and cross beds underlined by scattered pebbles. (p) Facies 12 (unit 4): conglomerate with an erosional basal surface and winnowed gravels at the top.

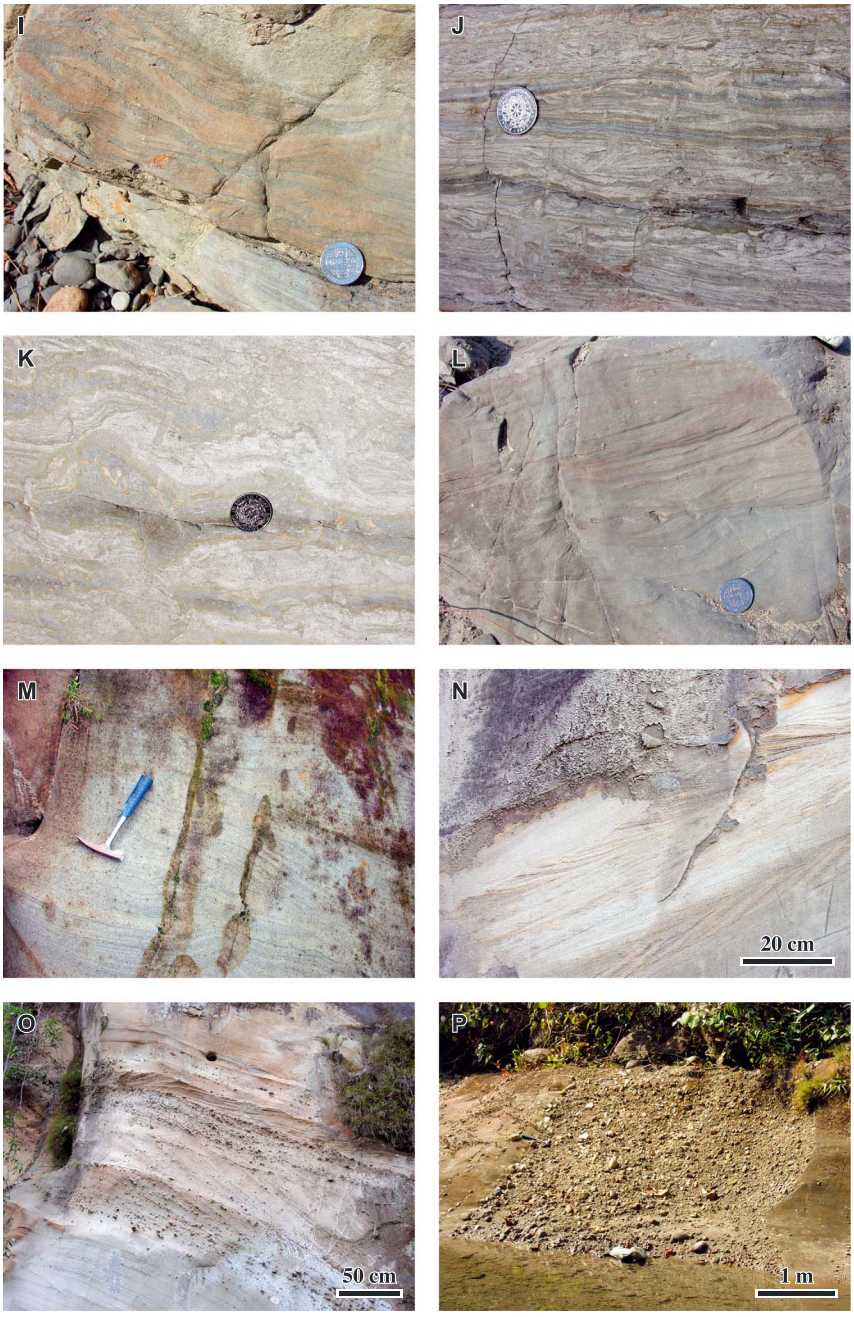

Figure 11. (continued)

5. Palynology

To constrain the local paleoclimate and complement our understanding of the paleodepositional environment, we have looked for the palynological content of the sediments at Dungsam Chu. Sampling strategy and analytical procedure are described in Text S4 in the supporting information [*Hoorn et al.*, 2000; *Traverse*, 1988].

In this exploratory palynological study of the Siwaliks sediments in Bhutan we have listed the sporomorphs by their botanical affinity, or with a form generic name, or morphological indication and type number (see caption Figure 13; Table D1). The taxa were further grouped into four main categories (Poaceae, other herbs, angiosperms/gymnosperms, and pteridophytes; see Table 5), in order to compare the Dungsam section with

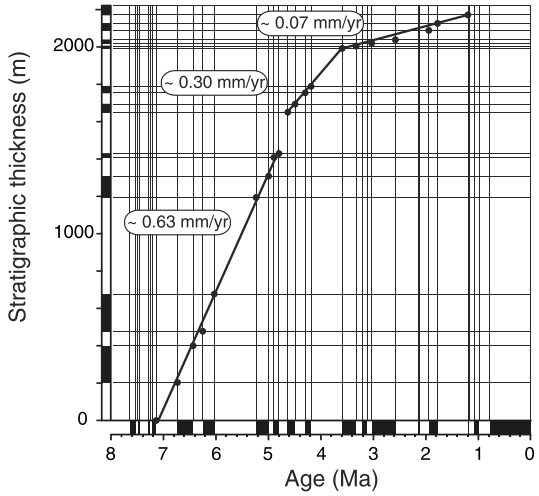

Figure 12. Age versus depth plot of the Dungsam Chu section using the correlation from Figure 9c.

the Surai Khola section in Nepal [*Hoorn et al*., 2000] (Figure S2). Overall, the pollen diversity is high with over 100 form genera (Table S3) observed in 16 samples (for sample location, see Figure 3b). Pre-Cenozoic sporomorphs were uncommon and listed under "corroded/indeterminate sporomorphs" in Table S3. This was not expected, given the deltaic (i.e., river-influenced) nature of the depositional environment and the common occurrence of these forms in Siwalik deposits documented elsewhere (e.g., in West Bengal [*More et al*., 2016]). This suggests that sediment reworking has had no marked influence on the pollen composition of the Dungsam Chu section.

Ferns and fern allies (Pteridophytes) are very abundant and range mostly from 50 to 75% throughout the section (Tables S3 and 5 and Figure 10d). They are indicative of humid, wet local conditions and are often found in the presence of a mountain forest. *Bhattarai et al*. [2004] have demonstrated that in Nepal, the maximum fern richness along the topographic gradient is found at around 2000 m and that at these elevations, ferns are strongly dependent on moisture and do not tolerate frost. The presence of *Ceratopteris* and *Selaginella* (Table S3) is also typical for open freshwater conditions.

Poaceae are frequent (5–25%), with peak occurrences (~50%) in the lower part of environmental unit 2 (Tables S3 and 5 and Figure 10d). Peaks of Asteraceae occurrence (5%) coincide with the Poaceae record. In contrast with findings in Pakistan [*De Franceschi et al*., 2008], the Bhutanese record presents low abundance to absence of *Chenopodiaceae-Amaranthaceae* in the Dungsam Chu samples, which is a group of wide ecological range, but particularly common in arid environments.

Taxa of broadleaved, deciduous forest, such as *Alnus*, *Betula*, *Corylus*, *Myrica*, and Fagaceae (Table S3), occur throughout the section but in relatively low abundances which, combined with the presence of taxa from high elevations (Ericaceae), suggest the presence of a broadleaved, deciduous forest over a pronounced topographic gradient.

The presence of tropical lowland taxa such as Sapotaceae, Anacardiaceae, Bombacoideae, and Rubiaceae is representative of the pollen influx from a lowland, evergreen rain forest. In contrast, the tree pollen referred to as "other Angiosperms/Gymnosperms" in Figure 10c, from unit 2, suggests less open vegetation until the top of the section.

Finally, there are punctuated single occurrences of mangrove to back-mangrove taxa indicative a coastal setting such as *Brownlowia* in the bottom half of unit 2. *Brownlowia* may also occur in tidally influenced freshwater swamps along the coastal plain [*Morley*, 1991; *Tomlinson*, 1994]. In addition, several single occurrences of palm tree-type pollens such as *Nypa* and the extinct *Neocouperipollis* representing palms from the coastal environment, and extending toward tidally influenced rivers and freshwaters swamps further inland [*Giesen et al*., 2007; *Monga et al*., 2015], are observed along the entire section (Table S3).

6. Discussion

6.1. Age of the Siwalik Group

Magnetostratigraphic results suggest that along the Dungsam Chu, the age of the base of the section is at ~7 Ma (Figure 9c), the boundaries between the classic lithological subgroups of the Siwalik Group being determined at ~6 Ma for the lower to middle Siwalik subgroups and at ~3.8 Ma for the middle to upper


1
10 µm
2
10 µm
3
4
5
6
10 µm
7
8
9
10
11
12
13
14
15a
15b
16
17
10 µm
18a
18b
19
20a
20b
21
22
10 µm
23
24
25
26
27
28a
28b
29
10 µm
30a
30b
31
32
33a
33b
33c
34a
34b
35a
35b
36a
36b
36c
37
38a
38b
38c
39
40
10 µm

Figure 13

Figure 13. (continued)

Figure 13. Optical micrographs of representative sporomorph taxa of the Neogene-Pleistocene Dungsam Chu section, Bhutan. The sample number and England Finder reference are given for each specimen. (1) *Magnolia* type; slide PN28-4; EF: E18-F18. (2) Reworked bisaccate; slide PN51-4; EF: U24-25/4-3. (3) Poaceae; slide PN85-4; EF: S30. (4) *Platanus*? (Type 39); slide PN85-4; EF: D22-4. (5) Myricoid-Betuloid type; slide PN21A-4; EF: Q33-3. (6) Myricoid-Betuloid type; slide PN21A-4; EF: T16-2. (7) *Nypa* (Type 38); slide PN21-4; EF: S13-3. (8) *Nypa* (Type 38); slide PN37-4; EF: R26-3. (9) *Neocouperipollis* (Type 36); slide PN37-4; EF: P12-2. (10) Meliaceae (Type 9); slide PN20A-4; EF: O34-3 (see also PN28-4; R31). (11) *Corylus* (Types 48 and 55); slide PN14B-4; EF: K-L23. (12) Juglandaceae/Pandaceae? (Type 19); slide PN28-4; EF: Q13-14/4-3. (13) *Carpinus*? (Type 63); slide PN85-4: U20-3. (14) *Alnus*; slide PN13A-4; EF: M22-23. (15a-b). Rubiaceae (Types 7 and 25); slide PN28-4; EF: T-U18. (16) Rubiaceae? (Type 6); slide PN20A; EF: E-F18/3-1. (17) *Quercus*; slide PN85-4; EF: H31. (18a-b) *Alangium* (Type 10); slide PN20A; EF: Q35-2. (19) Reticulate, tricolporate (Type 66); slide PN85-4; M20/1-2. (20a-b) Reticulate, tricolporate (Type 66); slide PN85-4; EF: W-V27-28. (21) Myrtaceae; slide PN13A-4: EF: M26. (22) Malvaceae? (Type 52); slide PN14B; EF: O20-4. (23) *Nypa* (Type 50); slide PN14B; EF: L-M/23-24. (24) Asteraceae; slide PN20A; EF: K34-1. (25) Asteraceae, *Centaurea* type; slide PN21-4; EF Q-R/31/3-1. (26) Asteraceae? slide PN20A; EF: J18. (27) Sapotaceae? (Type 65); slide PN85-4; EF: V25/1-2. (28a-b) Sapotaceae (Type 87-91); slide PN60-4; EF: S31-1. (29) *Brownlowia* (Type 18); slide PN28-4; EF: Q25-26/2-1. (30a-b) *Alangium* (Type 42); slide PN37-4; EF: X23-3. (31) Acanthaceae, *Justicia* type (Type 75); slide PN51A-4; EF: L19-1. (32) *Oncosperma* (Types 21 and 47); slide PN28-4; EF: R25/1-3. (33a-c) Anacardiaceae? (Type 32); slide PN37; EF: L28. (34a-b) *Mitragyna*, Rubiaceae; slide PN60-4; EF: N31-32. (35a-b) Reticulate, tricolpate indet.; slide PN60-4; EF: L32-3. (36a-c) Rubiaceae, reticulate, triporate (Types 74 and 86); slide PN60-4; EF: M28. (37) Rubiaceae, reticulate, and triporate (Types 74 and 86); slide PN55-4; EF: K-L/33-34. (38a-c) Verrucate and tricolporate (Type 61); slide PN85-4; EF: P27-3. (39) Caesalpiniaceae? (Type 73); slide PN51A-4; EF: M27-2. (40) Caesalpiniaceae? (Type 73); slide PN51A-4; EF: H-J28/4-2. (41) Indeterminate sporomorph; Slide PN28-4; E: O15-3? (42) Monolete spore; slide PN20A; EF: E24-3. (43) Polypodiaceae; slide PN85-4; J23 and J28-29. (44) *Nephrolepis*, Davalliaceae; slide PN20A; EF: N15. (45) *Stenochlaena palustris*, Blechnaceae; slide PN85-4; EF: U29/1-2. (46) *Pteris* type, Pteridaceae (Type 60); slide PN85-4; EF: N15-2. (47) *Pteris* type, Pteridaceae (Type 11); slide PN20A; EF: Q16-3. (48) *Pteris* type, Pteridaceae (Type 30); slide PN21A-4: EF: Q25-2. (49) *Selaginella*? (Type 77); slide PN31A-4; EF: N24-4. (50) *Selaginella* (Type 62); slide PN85-4; EF: R26-27/4-3. (51a-b) Verrucate/gemmate, trilete (*Microlepia*?) (Type 37); slide PN37-4; EF: Q-R16/4-2. (52) *Lycopodium cernuum* type (Type 34); slide PN37-4; EF: P21/2-4. (53) *Praedapollis* sp. (Type 35); slide PN37-4; EF: P19-1 and S30-2. (54) *Pteris* type, Pteridaceae (Type 33); slide PN37-4; EF: O20-1. (55a-b) *Ceratopteris*, Pteridaceae; slide PN21A-4; EF: Q32-2. (56) Bryophyte/Hepatic spore? (Type 51); slide PN14B; EF: O21-3.

Table 5. Summary of the Palynological Group Counts[a]

	PN13	PN14	PN20	PN21	PN28	PN31	PN37	PN51	PN55	PN58	PN60	PN65	PN74	PN82	PN85	PN86
Stratigraphic thickness (m)	252	297	398	416	568	630	666	854	1032	1067	1081	1158	1366	2180	2205	2209
Poaceae	6	23	185	182	13	10	29	27	32	8	39	21	11	33	16	21
Asteraceae	1		22	27		1					1			1	1	
Other Angiosperms/ Gymnosperms	18	26	43	48	26	29	27	59	38	9	72	46	42	47	51	38
Pteridophytes	86	144	81	95	240	87	91	28	116	56	89	111	39	169	107	58
SUM	**111**	**193**	**331**	**352**	**279**	**127**	**147**	**114**	**186**	**73**	**201**	**178**	**92**	**250**	**175**	**117**
Pteridophytes indeterminate	2	26	10	18	7	7	3	9	8	2	6	6	4	37	24	5
All corroded/indeterminate	20	43	34	37	23	18	28	100	47	18	34	35	15	81	53	10

[a]Boldface highlights the sum for each column.

Siwalik subgroups, while the top of the section is ~1 Ma (Figures 9c and 10). Previous magnetostratigraphic correlations in the Neogene-Quaternary Himalayan foreland basin from Pakistan to Arunachal Pradesh document ages ranging from 8 to 12 Ma for the lower to middle Siwalik transition [e.g., *Chirouze et al*., 2012; *Gautam and Fujiwara*, 2000; *Ojha et al*., 2000, 2009; *Tokuoka et al*., 1986] and from 2 to 3.5 Ma for the middle to upper Siwalik transition [e.g., *Behrensmeyer et al*., 2007; *Ojha et al*., 2009; *Sanyal et al*., 2004] (Figure 14a). Therefore, in the Dungsam Chu section, the boundary between the lower and middle Siwalik subgroups is 2 to 6 Ma younger than documented elsewhere along the Himalayan arc. Furthermore, the duration of deposition of the middle Siwalik subgroup varies from 3 to 6 Ma in central and western Nepal (Surai and Muksar Khola sections) [*Ojha et al*., 2009] to about 2–3 Ma in Bhutan (Dungsam Chu section) to as long as 8 Ma in Arunachal Pradesh (Kameng section, Figure 14a) [*Chirouze et al*., 2012]. Apparently, the Kameng section differs significantly from the Nepalese and Bhutanese sections (Figure 14a) although these differences are not straightforward to explain.

Indeed, it has been clearly demonstrated that vertical transitions between lithostratigraphic formations and their lateral diachroneity cannot be interpreted simply in terms of tectonic and climatic forcing, especially in foreland basins [e.g., *Barberà et al*., 2001; *Burbank et al*., 1986; *Charreau et al*., 2009; *Heermance et al*., 2007]. These changes reflect the 4-D space-time evolution of depositional profiles documented by one-dimensional vertical sections located at different positions, more proximal or more distal, with respect to the mountain range and its foreland. Consequently, extensive and careful spatiotemporal constraints, both parallel and perpendicular to the orogenic system, are necessary to properly discuss what controls the vertical and lateral transitions between the lithostratigraphic formations in a foreland basin. Additionally, a sedimentological and stratigraphical reading of such variations in terms of paleoenvironmental, paleogeographical, and sequential evolution is often more pertinent than a strictly lithostratigraphic approach.

6.2. Depositional Environments and Paleogeography

The Siwalik Group in Bhutan shows an overall distal to proximal trend as observed everywhere else in the Himalayan foreland basin [e.g., *Chirouze et al*., 2012; *DeCelles et al*., 1998b; *Kumar et al*., 2003; *Nakayama and Ulak*, 1999]. This long-term progradational trend, which is typical of the filling sequence of foreland basins at their active margin [e.g., *Jordan*, 1995; *Puigdefàbregas et al*., 1986; *Schlunegger et al*., 1997; *Sinclair and Allen*, 1992; *Stockmal et al*., 1992], is controlled by the propagation of the deformation front, generally together with an increasing erosion and sediment flux, related to the horizontal and vertical growth of the adjacent mountain range.

To the west of the system, the sedimentary paleoenvironments are thus interpreted as meandering and braided fluvial depositional systems (lower and middle Siwalik subgroups) grading into alluvial fan systems (upper Siwalik subgroup) (Figure 14b). This kind of environmental evolution is uniformly observed from Pakistan [*Abbasi and Friend*, 2000; *Willis*, 1993; *Zaleha*, 1997] to western India [*Brozovic and Burbank*, 2000; *Johnson et al*., 1983; *Kumar et al*., 2003, 2004; *Suresh et al*., 2004] and Nepal [*DeCelles et al*., 1998b; *Huyghe et al*., 2005; *Nakayama and Ulak*, 1999; *Ojha et al*., 2009]. In some places, floodplains with intermittent lacustrine conditions attributed to seasonal flooding are also recorded [*DeCelles et al*., 1998b; *Hoorn et al*., 2000] but always in a continental environment.

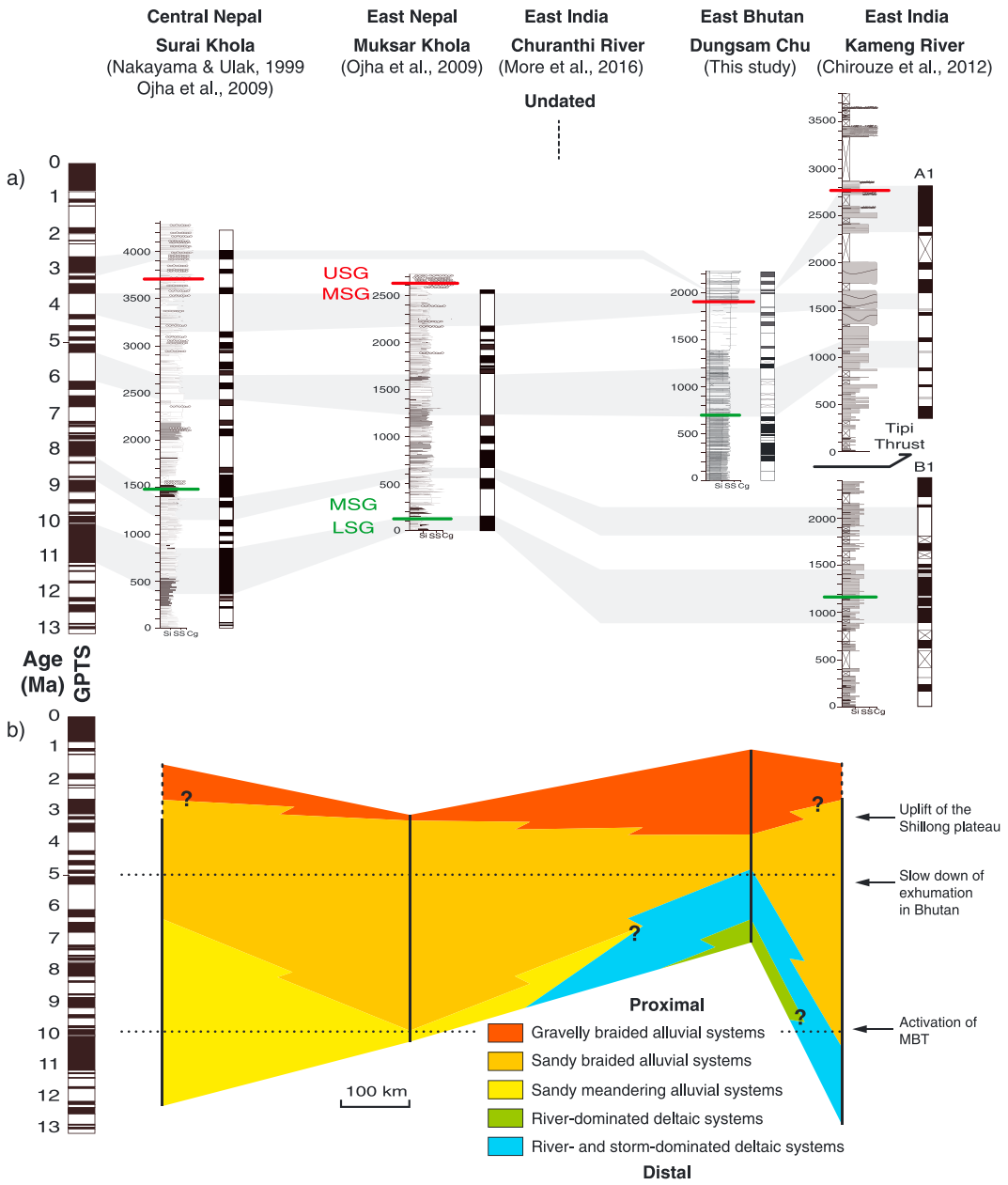

Figure 14. (a) Summary of magnetostratigraphic correlations to the GPTS of stratigraphic sections of Siwalik deposits along the eastern Himalayan arc (modified after *Hirschmiller et al.* [2014]). USG: upper Siwalik subgroup, MSG: middle Siwalik subgroup, LSG: lower Siwalik subgroup. Si, SS, and Cg are abbreviations for siltstone, sandstone, and conglomerate. (b) Lateral variations of depositional environments. Stratigraphic sections are from *Nakayama and Ulak* [1999] and *Ojha et al.* [2009] (Surai and Muksar Khola), this study (Dungsam Chu), and *Chirouze et al.* [2012] (Kameng River).

A paleoenvironmental change occurs east of Nepal where thick deltaic deposits appear in the lower and middle Siwalik subgroups (Figure 14b). Along the Churanthi River in West Bengal (Figure 1), brackish water to shallow marine conditions are documented by palynological data and trace fossils in the undated middle Siwalik subgroup [*More et al.*, 2016]. Farther east, our observations indicate that along the Dungsam Chu, the basal environmental units 1 and 2 correspond to deposits of a river-dominated deltaic system and a wave-influenced deltaic environment, respectively, associated with marine trace fossils, glauconite, and some coastal pollen taxa, suggesting a marine setting before ~5 Ma (Figure 14b). After that, the deposits grade to units 3 and 4, which represent a sandy and a gravelly alluvial system, respectively. Along the Kameng section in Arunachal Pradesh (Figure 1), *Chirouze et al.* [2012] also describe a lacustrine to marine deltaic environment

in the lower Siwalik subgroup (Dafla Formation) before ~10.5 Ma (Figure 14b). Moreover, the overlying braided river sediments of the middle Siwalik subgroup (Subansiri Formation) and alluvial fan deposits of the upper Siwalik subgroup are reported to both bear paleobotanical evidences of brackish water or near coastal environments [e.g., *Chirouze et al*., 2012; *Mehrotra et al*., 1999; *Singh and Tripathi*, 1990]. We speculate that these brackish water to shallow marine paleoenvironments are linked to those observed to the northeast of the Shillong Plateau in the foreland of the Naga Hills of Assam [e.g., *Bhandari et al*., 1973; *Reimann and Hiller*, 1993] and to the south in the well-dated Surma Basin of northern Bangladesh [e.g., *Alam et al*., 2003; *Najman et al*., 2012; *Worm et al*., 1998] (Figure 1).

In the foreland of the Naga Hills in Assam, paleoenvironmental data indicate marine influence during the Neogene, although the chronological constraints on sediment deposition remain poorly constrained [*Bhandari et al*., 1973; *Evans*, 1932; *Mallet*, 1876; *Reimann and Hiller*, 1993]. The Miocene Surma Group displays fossil assemblages pointing toward shallow marine to brackish water environments, whereas the overlying Mio-Pliocene Tipam Group is characterized by lithologic characteristics and floral assemblages symptomatic of a fluvial environment in a subtropical to temperate climate [e.g., *Bhandari et al*., 1973; *Reimann and Hiller*, 1993].

The Surma Basin in Bangladesh also records nearshore to marine conditions in strata contemporaneous with the marine facies recorded in Bhutan [e.g., *Johnson and Nur Alam*, 1991]. The latest Miocene-Pliocene Surma Group consists of the Bhuban and Bokabil Formations. The Bhuban Formation displays a proximal marine deltaic system associated with mangrove taxa and is interlayered with shallow marine incursions. The overlying Bokabil Formation is characterized by the presence of foraminiferal tests associated with mangrove taxa. The top of the Surma Group is characterized by the Upper Marine Shale, which represents the final marine incursion to this area, dated at 2.5–3.9 Ma. Above this, the overlying Tipam and Dupi Tila Formations were then deposited in a fluvial environment [e.g., *Gani and Alam*, 2004; *Johnson and Nur Alam*, 1991; *Najman et al*., 2012; *Worm et al*., 1998].

There are extensive lateral variations in lithologies and thicknesses of the different sediment sequences described in those different areas, some of them located quite far (a few hundred kilometers) from the Dungsam Chu section. However, we speculate that the observations collectively suggest that the marine incursions emanating from the Bay of Bengal to the south and recorded both in the Naga Hills and the Surma Basin until the deposition of fluvial facies from ~3.9 Ma may have had a peripheral impact on the facies observed at the front of the Himalayan range in eastern India [*Chirouze et al*., 2012; *More et al*., 2016] and in Bhutan until at least ~5 Ma. Our hypothesis supports a post-Miocene full continentalization of the eastern Himalayan foreland basin, much later in time than previously suggested in this area [e.g., *Alam et al*., 2003; *Johnson and Nur Alam*, 1991] and than farther west. In Nepal the peripheral foreland basin shows clear evidence for an extensive unconformity separating marine facies below and fluvial facies above [*Decelles et al*., 1998a]. The youngest marine facies are generally considered to be Mid-Eocene in age although this matter remains debated [e.g., *Bhatia and Bhargava*, 2006; *Najman*, 2007], while the fluvial facies commenced, at the latest, by 20 Ma [*Ojha et al*., 2009; *White et al*., 2002], which is at least 15 Ma earlier than observed in Bhutan.

The post-Miocene continentalization of the Dungsam Chu region and the eastern Himalayan foreland basin likely result from a combination of two main factors including (1) the long-term progradation of the foreland depositional landscape related to the growth of the Himalayan orogenic wedge, which has probably produced a southward migration of the shoreline of the Bay of Bengal, and (2) the long-term sea level fall initiated since the late Miocene [*Hansen et al*., 2013; *Miller et al*., 2005]. Superimposed on this second-order eustatic trend, a relative sea level high occurred before 4.9 Ma [*Hansen et al*., 2013; *Miller et al*., 2005] which potentially has promoted a marine influence in our study area until the wave-influenced deltaic environment changed for a river-dominated environment. Finally, the deformation and surface uplift of the Shillong block must have decreased the subsidence of the eastern Himalayan foreland before creating a topographic barrier into the basin after 4–3 Ma [*Biswas et al*., 2007; *Najman et al*., 2016]

6.3. Palynology and Paleoclimate

The predominance of grass and fern sporomorphs and a highly diverse assemblage of angiosperms and pteridophytes, which collectively are typical for tropical lowland vegetation, characterize the composition

of the palynological assemblage in the Dungsam Chu section. In essence, this assemblage is comparable to the palynological results obtained in central Nepal along the Surai Khola [*Hoorn et al*., 2000] (Figure S2), but the larger variety of lowland taxa in eastern Bhutan suggests a more diverse tropical lowland vegetation upstream of the sedimentary basin.

In terms of temporal evolution, the composition of the palynological assemblage does not significantly change through the 7–1 Ma interval documented by the Dungsam Chu section. In contrast, the Surai Khola section shows a shift at around 6.5 Ma, when ferns drop and grasses predominate from then onward [*Hoorn et al*., 2000]. The Bhutanese record thus resembles the pre-6.5 Ma Nepalese record, rather than its post-6.5 Ma temporal equivalent (Figure S2). This suggests that the environment and probably the paleoclimate in Bhutan, in the lowland and floodplain, were consistently more humid than the coeval environments and paleoclimate in Nepal, as is the case nowadays [*Bookhagen and Burbank*, 2010, 2006]. The palynological record thus indicates that the orographic perturbation of ISM precipitations exerted by the surface uplift of the Shillong Plateau 4–3 [*Biswas et al*., 2007] to 3.5–2 Ma ago [*Najman et al*., 2016] did not measurably modify the wet local climate observed in the Bhutanese foothills since 7 Ma.

6.4. Accumulation Rates and Deformation

In foreland basins, the rates of sediment preservation are conditioned by the spatiotemporal evolution of the subsidence, which primarily generate accommodation space for deposits, and by sediment supply derived from the erosion of the adjacent mountain range [*DeCelles and Giles*, 1996]. Consistent with the forelandward migration of the basin flexure associated with the lateral and vertical growth of the orogenic system, the foredeep depozones of foreland basins are generally characterized by an overall acceleration of subsidence through time recorded by increasing accumulation rates and convex up subsidence curves [e.g., *Charreau et al*., 2009; *Ojha et al*., 2009; *Xie and Heller*, 2009]. For the Himalayan foreland basin, such increasing or constant accumulation rates calculated from the nondecompacted sedimentary thicknesses of the Siwalik deposits have been mostly interpreted in terms of flexure associated with the slip history of the Main Boundary Thrust (MBT) [e.g., *Burbank et al*., 1996; *Meigs et al*., 1995; *Ojha et al*., 2009]. Contrary to other foreland sedimentary sections from Pakistan to Arunachal Pradesh [see *Ojha et al*., 2009, Figure 13;*Chirouze et al*., 2012, Figure 10], the Dungsam Chu section has a unique characteristic which is that the accumulation rate decreases steadily from ~0.63 mm/yr between ~7 and ~4.5 Ma to ~0.3 mm/yr between ~4.5 and ~3.5 Ma and ~0.07 mm/yr between ~3.5 and ~1 Ma (Figures 10c and 12).

Different mechanisms including climatically or tectonically driven decrease in subsidence and/or in sediment supply to the foreland basin may potentially account for this deceleration of accumulation rate in eastern Bhutan. First, the detrital influx entering the basin may have decreased due to a climatically driven slowdown of erosion in the hinterland of the orogen. Second, a tectonically driven decrease in subsidence could have resulted from the forelandward propagation of the fold-and-thrust belt and the integration of the study area into the thrust-wedge depozone of the basin. Third, the subsidence and/or the sediment supply may have diminished due to a tectonically driven decrease of shortening rates along the frontal Himalayan structures generating decay of crustal thickening and erosion in the hinterland and decay of the lithospheric flexure in the foreland.

First, in Bhutan, a decrease in detrital influx may have resulted from a climatically driven slowdown of erosion in the range during the Pliocene [*Grujic et al*., 2006], in response to the surface uplift and orographic effect of the Shillong Plateau [*Biswas et al*., 2007]. Yet the lack of paleoclimatic changes in our palynological data and the steady stable isotopic record from authigenic clay minerals across the stratigraphic section (Grujic, personal communication of unpublished data, 2016) refute this hypothesis.

Second, a tectonically driven decrease in subsidence in relation with the propagation of the deformation front toward the foreland could also be plausible. Indeed, the Dungsam Chu section has migrated from the foredeep to the wedge-top depozone of the basin [e.g., *DeCelles and Giles*, 1996], since it is currently located in the hanging wall of the Main Frontal Thrust (MFT) (Figure 2). Therefore, the time at which this thrust was activated becomes of critical importance. Based on detrital thermochronology and/or the presence of growth strata, ongoing displacement on the MFT is suggested to have started ~2 Ma ago in western and central Nepal [*Mugnier et al*., 2004; *van der Beek et al*., 2006] and ~1 Ma ago in eastern India in Arunachal Pradesh [*Chirouze et al*., 2013] and possibly at an unspecified younger time [*Burgess et al*., 2012], while the timing

remains undetermined in Bhutan. However, the accumulation rates at Dungsam Chu have decayed since at least 4.5 Ma. Given the post ~2–1 Ma MFT activation documented along the eastern Himalayan arc, it hence seems reasonable to assume that during most of its deposition, the Dungsam Chu section remained located in the foredeep depozone and has not experienced a reduced creation of accommodation space due to the forelandward propagation of the Himalayan deformation front (MFT) before the Pleistocene.

Third, the last option available to explain the deceleration of accumulation rates observed in eastern Bhutan is a tectonically driven decrease in subsidence and/or detrital influx due to a change in the deformation of the range and its foreland. What makes the Dunsgam Chu section special along the Himalayan arc is its location north of the Shillong Plateau, a unique basement-cored uplift in the Himalayan foreland (Figure 1). At the longitude of central and eastern Bhutan, the Himalayan foreland corresponds to a broken foreland basin [e.g., *Jordan*, 1995; *Strecker et al*., 2012], rather than a classical foreland system [e.g., *DeCelles and Giles*, 1996]. In this area, the foredeep is very shallow (maybe <1 km), in contrast to areas west and east of Bhutan (depths >4 km) [*Dasgupta*, 2000; *Verma and Mukhopadhyay*, 1977; *Vernant et al*., 2014, Figure 1b].

The exhumation/cooling of the Shillong Plateau's basement initiated 9–15 Ma ago [*Biswas et al*., 2007; *Clark and Bilham*, 2008] and its surface uplift 3–4 Ma [*Biswas et al*., 2007] to 3.5–2 Ma ago [*Najman et al*., 2016]. Both likely have had a significant influence in a reorganization of the regional paleogeography and the partitioning of India-Eurasia convergence along the Bhutanese range front. Based on thermokinematic modeling of thermochronometric data tied to a sequential balanced cross section, *McQuarrie and Ehlers* [2015] suggested that in the LHS of eastern Bhutan, shortening rates decreased between 8 and 0 Ma. Inverting a thermochronometric data set using 3-D thermokinematic modeling, *Coutand et al*. [2014] inferred a 50% decrease in long-term exhumation rates at ~6 Ma in eastern Bhutan. At the time, *Coutand et al*. [2014] were not able to differentiate whether this drop in erosion rate should be attributed to climatic- or tectonic-related processes. Because in the Dungsam Chu section there is a lack of change of both the palynological record (Figures 10d and Table S3) and stable isotope climatic proxies (Grujic, personal communication of unpublished data, 2016) after 6.5 Ma (for most of the section deposition), we contend that tectonics had a prominent influence on the nature and magnitude of the foreland basin filling in eastern Bhutan. The onset of the Shillong block's deformation and the slowdown of the displacement rates along the MBT in eastern Bhutan during the latest Miocene-Pleistocene would have had a direct impact on the accommodation space created in the basin, as well as on the detrital influx derived from the Himalayan orogenic wedge, decreasing them both.

In the northeastern corner of India, plate reconstruction suggests that the convergence between India and Eurasia has been 44 mm/yr over the past ~11 Ma [*Molnar and Stock*, 2009], out of which GPS measurements indicate that a contraction of 14–17 mm/yr [*Vernant et al*., 2014] is currently accommodated in Bhutan. The discrepancy observed between long-term (0.65–2.9 mm/yr over the last 10 Ma [*Biswas et al*., 2007; *Clark and Bilham*, 2008]) and short-term (3–7 mm/yr [*Vernant et al*., 2014]) contraction rates accommodated on the Dauki Fault suggests that the amount of horizontal shortening accommodated by the Shillong Plateau has increased during the last 10 Ma, while it has concomitantly decreased by 3–8 mm/yr in the Bhutan Himalaya [*Vernant et al*., 2014]. We hence attribute the late Miocene-Pleistocene decrease in sedimentary accumulation rates observed in eastern Bhutan to a tectonically driven change in subsidence and/or detrital influx in the basin, in response to an increasing partitioning of the India-Eurasia total convergence into the Shillong Plateau.

7. Conclusions

This multidisciplinary study of the exposed Siwalik Group along the Dungsam Chu in eastern Bhutan leads to the following conclusions:

1. Magnetostratigraphy constrained by vitrinite reflectance and detrital AFT data indicate that the Siwalik Group was deposited during the latest Miocene and the Pleistocene, between ~7 Ma and ~1 Ma.
2. Depositional environments include river-dominated and wave-influenced deltaic systems at the base which, associated with marine trace fossils, glauconite, and some coastal pollen taxa, suggest a marine setting potentially linked to marine incursions from the Bay of Bengal. At around 5 Ma, a transition to a sandy and then gravelly alluvial environment occurs. Together with the sedimentological observations in eastern India (West Bengal, Arunachal Pradesh, and Assam) and northern Bangladesh, this paleoenvironmental evolution is consistent with a post-Miocene complete continentalization of the eastern Himalayan foreland basin at least 15 Ma later than is observed in the western Himalayan foreland basin.

3. The sporomorphs represent taxa from different vegetation types in the proximal Himalayan orogenic system and point to diverse tropical lowlands and rain forest vegetation throughout the ~7–1 Ma time period. The palynological record also indicates that depositional environments and paleoclimate were consistently more humid in Bhutan than the coeval in Nepal. This is similar to modern precipitation patterns along the strike of the Himalaya, which are characterized by an east-to-west decrease in ISM precipitation intensity. Furthermore, no major change in moisture or temperature is documented in Bhutan between 7 and 1 Ma, indicating that the orographic blockage of ISM precipitations exerted by the surface uplift of the Shillong Plateau 3.5–2 Ma ago did not measurably modify the wet local climate documented in the Bhutanese foothills since 7 Ma.
4. During the last 7 Ma, the sustained decrease in accumulation rates of the Siwalik Group sediments in the Dungsam Chu section results from a progressive diminution of the flexural subsidence in the basin and/or of the detrital input from the range, which we attribute to the onset of the Shillong block's deformation and a slowdown of the displacement rates along the MBT in eastern Bhutan during the latest Miocene-Pleistocene, in response to an increasing partitioning of the India-Eurasia convergence into the Shillong Plateau.

Acknowledgments

Fieldwork was supported by the France-Stanford Foundation (I.C.) and the Natural Sciences and Engineering Research Council of Canada (discovery grant RGPIN 371671 to I.C. and RGPIN 04297 do D.G.). I.C. thanks ETH Zürich for financial support (visiting professorship grant) during the writing of the manuscript. G.G. and Y.N. acknowledge financial support from a Marie Curie Initial Training Network iTECC funded by the EU REA under the FP7 implementation of the Marie Curie Action, under grant agreement 316966. C. Hoorn thanks the Hugo de Vries-Fonds (http://www.hugodevriesfonds.nl/) for financial support and R. Morley, K. Richards, and K. Paudayal for assisting her with the identification of selected pollen and spores. We thank A. Philip for the palynological processing and J. van Arkel for microphotography. The work of L. Barrier for this publication is the IPGP contribution 3665. The new data sets presented in this manuscript are available in Tables 1–5 in the main text and in Texts S1–S4 in supporting information.

References

Abbasi, I. A., and P. F. Friend (2000), Exotic conglomerates of the Neogene Siwalik succession and their implications for the tectonic and topographic evolution of the western Himalaya, *Geol. Soc. Spec. Publ.*, *170*, 455–466.

Adams, B., K. Hodges, K. Whipple, T. Ehlers, M. Soest, and J. Wartho (2015), Constraints on the tectonic and landscape evolution of the Bhutan Himalaya from thermochronometry, *Tectonics*, *34*, 1329–1347, doi:10.1002/2015TC003853.

Alam, M., M. Alam, J. Curray, M. Chowdhury, and M. Gani (2003), An overview of the sedimentary geology of the Bengal Basin in relation to the regional tectonic framework and basin-fill history, *Sediment. Geol.*, *155*(3), 179–208.

American Society for Testing and Materials (2010), D2798-09a: Standard test method for microscopical determination of the vitrinite reflectance of coal, in *Annual Book of ASTM Standards: Petroleum Products, Lubricants, and Fossil Fuels; Gaseous Fuels; Coal and Coke*, edited, pp. 406–410, ASTM Int., West Conshohocken, Pa.

Auden, J. (1935), Traverse in the Himalaya, *Rec. Geol. Surv. India*, *69*(2), 123–167.

Barberà, X., L. Cabrera, M. Marzo, J. Parés, and J. Agustí (2001), A complete terrestrial Oligocene magnetobiostratigraphy from the Ebro Basin, Spain, *Earth Planet. Sci. Lett.*, *187*(1), 1–16.

Barker, C., and M. Pawlewicz (1994), Calculation of vitrinite reflectance from thermal histories and peak temperatures: A comparison of methods, in *Vitrinite Reflectance as a Maturity Parameter*, edited by P. Mukhopadhyay and W. Dow, pp. 216–229, Am. Chem. Soc, Symposium Ser., Washington, D. C.

Behrensmeyer, A., et al. (2007), The structure and rate of late Miocene expansion of C4 plants: Evidence from lateral variation in stable isotopes in paleosols of the Siwalik Group, northern Pakistan, *Geol. Soc. Am. Bull.*, *119*, 1486–1505.

Bhandari, L. L., R. C. Fuloria, and V. V. Sastri (1973), Stratigraphy of Assam Valley, India, *Am. Assoc. Pet. Geol. Bull.*, *57*(4), 642–654, doi:10.1306/819A4310-16C5-11D7-8645000102C1865D.

Bhargava, O. N. (1995), *The Bhutan Himalaya: A Geological Account*, 245 pp., Geol. Surv. of India.

Bhatia, S., and O. Bhargava (2006), Biochronological continuity of the Paleogene sediments of the Himalayan Foreland Basin: Paleontological and other evidences, *J. Asian Earth Sci.*, *26*(5), 477–487.

Bhattarai, K. R., O. R. Vetaas, and J. A. Grytnes (2004), Fern species richness along a central Himalayan elevational gradient, Nepal, *J. Biogeogr.*, *31*(3), 389–400.

Bilham, R., and P. England (2001), Plateau "pop-up"in the great 1897 Assam earthquake, *Nature*, *410*(6830), 806–809.

Biswas, S., and B. Grasemann (2005), Quantitative morphotectonics of the southern Shillong Plateau (Bangladesh/India), *Austrian J. Earth Sci.*, *97*, 82–93.

Biswas, S., I. Coutand, D. Grujic, C. Hager, D. Stockli, and B. Grasemann (2007), Exhumation and uplift of the Shillong Plateau and its influence on the eastern Himalayas: New constraints from apatite and zircon (U-Th-[Sm])/He and apatite fission track analyses, *Tectonics*, *26*, TC6013, doi:10.1029/2007TC002125.

Bookhagen, B., and D. W. Burbank (2006), Topography, relief, and TRMM-derived rainfall variations along the Himalaya, *Geophys. Res. Lett.*, *33*, L08405, doi:10.1029/2006GL026037.

Bookhagen, B., and D. Burbank (2010), Toward a complete Himalayan hydrological budget: Spatiotemporal distribution of snowmelt and rainfall and their impact on river discharge, *J. Geophys. Res.*, *115*, F03019, doi:10.1029/2009JF001426.

Brandon, M. (1992), Decomposition of fission-track grain-age distributions, *Am. J. Sci.*, *292*, 535–564.

Brandon, M. (1996), Probability density plot for fission-track grain-age samples, *Radiat. Meas.*, *26*, 663–676.

Brandon, M. (2002), Decomposition of mixed grain age distributions using Binomfit, *On Track*, *24*, 13–18.

Brozovic, N., and D. W. Burbank (2000), Dynamic fluvial systems and gravel progradation in the Himalayan foreland, *Bull. Geol. Soc. Am.*, *112*(3), 394–412, doi:10.1130/0016-7606(2000)112<394:DFSAGP>2.0.CO;2.

Buatois, L. (2012), Sedimentological and ichnological signatures of changes in wave, river and tidal influence along a Neogene tropical deltaic shoreline, *Sedimentology*, *59*, 1568–1612, doi:10.1111/j.1365-3091.2011.01317.x.

Burbank, D., R. Raynolds, and G. Johnson (1986), Late Cenozoic tectonics and sedimentation in the northwestern Himalayan foredeep: II. Eastern limb of the Northwest Syntaxis and regional synthesis, in *Foreland Basins*, edited by P. Allen and P. Homewood, pp. 293–306, Blackwell Sci., Oxford, doi:10.1002/9781444303810.ch16.

Burbank, D., R. Beck, and T. Mulder (1996), The Himalayan foreland basin, in *Asian Tectonics*, edited by A. Yin and T. Harrison, pp. 149–188, Cambridge Univ. Press, Cambridge.

Burgess, W., A. Yin, C. Dubey, Z.-K. Shen, and T. Kelty (2012), Holocene shortening across the Main Frontal Thrust zone in the eastern Himalaya, *Earth Planet. Sci. Lett.*, *357*, 152–167.

Butler, R. (1992), *Paleomagnetism: Magnetic Domains to Geologic Terranes*, 319 pp., Blackwell Sci., Boston, Mass.
Chan, M., and R. Dott Jr. (1986), Depositional facies and progradational sequences in Eocene wave-dominated deltaic complexes, Southwestern Oregon, *AAPG Bull.*, *70*(4), 415–429.
Charreau, J., Y. Chen, S. Gilder, L. Barrier, S. Dominguez, R. Augier, S. Sen, J. P. Avouac, A. Gallaud, and F. Graveleau (2009), Neogene uplift of the Tian Shan Mountains observed in the magnetic record of the Jingou River section (northwest China), *Tectonics*, *28*, C2008, doi:10.1029/2007TC002137.
Chatterjee, N., A. Mazumdar, A. Bhattacharya, and R. Saikia (2007), Mesoproterozoic granulites of the Shillong–Meghalaya Plateau: Evidence of westward continuation of the Prydz Bay Pan-African suture into Northeastern India, *Precambrian Res.*, *152*(1), 1–26.
Chirouze, F., G. Dupont-Nivet, P. Huyghe, P. Van Der Beek, T. Chakraborti, M. Bernet, and V. Erens (2012), Magnetostratigraphy of the Neogene Siwalik Group in the far eastern Himalaya: Kameng section, Arunachal Pradesh, India, *J. Asian Earth Sci.*, *44*, 117–135.
Chirouze, F., P. Huyghe, P. van der Beek, C. Chauvel, T. Chakraborty, G. Dupont-Nivet, and M. Bernet (2013), Tectonics, exhumation, and drainage evolution of the eastern Himalaya since 13 Ma from detrital geochemistry and thermochronology, Kameng River Section, Arunachal Pradesh, *Geol. Soc. Am. Bull.*, *125*(3–4), 523–538.
Clark, M. K., and R. Bilham (2008), Miocene rise of the Shillong Plateau and the beginning of the end for the Eastern Himalaya, *Earth Planet. Sci. Lett.*, *269*(3), 337–351, doi:10.1016/j.epsl.2008.01.045.
Collinson, J. (1969), The sedimentology of the Grindslow Shales and the Kinderscout Grit: A deltaic complex in the Namurian of northern England, *J. Sediment. Petrol.*, *39*(1), 194–221.
Coutand, I., B. Carrapa, A. Deeken, A. Schmitt, E. Sobel, and M. Strecker (2006), Propagation of orographic barriers along an active range front: Insights from sandstone petrography and detrital apatite fission-track thermochronology in the intramontane Angastaco basin, NW Argentina, *Basin Res.*, *18*(1), 1–26.
Coutand, I., D. Whipp, D. Grujic, M. Bernet, M. Fellin, B. Bookhagen, K. Landry, S. Ghalley, and C. Duncan (2014), Geometry and kinematics of the Main Himalayan Thrust and Neogene crustal exhumation in the Bhutanese Himalaya derived from inversion of multithermochronologic data, *J. Geophys. Res. Solid Earth*, *119*, 1446–1481, doi:10.1002/2013JB010891.
Dasgupta, S. (2000), *Seismotectonic Atlas of India and Its Environs*, Geol. Surv. of India, Kolkota, India.
DeCelles, P., and K. Giles (1996), Foreland basin systems, *Basin Res.*, *8*, 115–153.
Decelles, P. G., G. E. Gehrels, J. Quade, and T. P. Ojha (1998a), Eocene-early Miocene foreland basin development and the history of Himalayan thrusting, western and central Nepal, *Tectonics*, *17*, 741–765, doi:10.1029/98TC02598.
DeCelles, P. G., G. E. Gehrels, J. Quade, T. P. Ojha, P. A. Kapp, and B. N. Upreti (1998b), Neogene foreland basin deposits, erosional unroofing, and the kinematic history of the Himalayan fold-thrust belt, western Nepal, *Geol. Soc. Am. Bull.*, *110*(1), 2–21.
De Franceschi, D., C. Hoorn, P.-O. Antoine, I. U. Cheema, L. J. Flynn, E. H. Lindsay, L. Marivaux, G. Métais, A. R. Rajpar, and J.-L. Welcomme (2008), Floral data from the mid-Cenozoic of central Pakistan, *Rev. Palaeobot. Palynol.*, *150*(1), 115–129.
Diehl, T., J. Singer, G. Hetényi, D. Grujic, J. Clinton, and E. Kissling (2016), The seismic gap of Bhutan: Evidence for segmentation of the Himalayas and its link to foreland deformation, paper presented at Himalayan-Karakorum-Tibet Workshop, Aussois, France, 9–12 May.
Donelick, R. A., P. B. O'Sullivan, and R. A. Ketcham (2005), Apatite fission-track analysis, *Rev. Mineral. Geochem.*, *58*(1), 49–94.
Dumitru, T. A. (1993), A new computer-automated microscope stage system for fission track analysis, *Nucl. Tracks Radiat. Meas.*, *21*, 575–580.
Evans, P. (1932), Tertiary succession in Assam, *Trans. Min. Geol. Inst. India*, *27*(3), 155–260.
Galbraith, R. (2005), *Statistics for Fission Track Analysis*, Chapman & Hall/CRC, Boca Raton, Fla.
Galbraith, R., and P. Green (1990), Estimating the component ages of a finite mixture, *Nucl. Tracks Radiat. Meas.*, *17*, 197–206.
Gani, M., and M. Alam (2004), Fluvial facies architecture in small-scale river systems in the Upper Dupi Tila Formation, northeast Bengal Basin, Bangladesh, *J. Asian Earth Sci.*, *24*(2), 225–236.
Gani, M., and J. Bhattacharya (2007), Basic building blocks and process variability of a Cretaceous delta: internal facies architecture reveals a more dynamic interaction of river, wave, and tidal processes than indicated by external shape, *J. Sediment. Res.*, *77*, 284–302, doi:10.2110/jsr.2007.023.
Gansser, A. (1983), *Geology of the Bhutan Himalaya*, 181 pp., Birkhaüser, Boston, Mass.
Gautam, P., and Y. Fujiwara (2000), Magnetic polarity stratigraphy of Siwalik Group sediments of Karnali River section in western Nepal, *Geophys. J. Int.*, *142*(3), 812–824.
Gautam, P., and W. Rösler (1999), Depositional chronology and fabric of Siwalik group sediments in Central Nepal from magnetostratigraphy and magnetic anisotropy, *J. Asian Earth Sci.*, *17*, 659–682.
Ghosh, S., D. Paul, J. Bhalla, P. Bishui, S. Gupta, and S. Chakraborty (1994), New Rb-Sr isotopic ages and geochemistry of granitoids from Meghalaya and their significance in middle-to late Proterozoic crustal evolution, *Indian Min.*, *48*, 33–44.
Giesen, W., S. Wulffraat, M. Zieren, and L. Scholten (2007), *Mangrove Guidebook for Southeast Asia*, FAO and Wetlands Int, Bangkok, Thailand.
Gradstein, F., and J. Ogg (2012), The chronostratigraphic scale, in *The Geologic Time Scale*, edited by F. M. Gradstein, J. G. O. D. Schmitz, and G. M. Ogg, pp. 31–42, Elsevier, Boston, Mass., doi:10.1016/B978-0-444-59425-9.00002-0.
Gradstein, F. M. (2012), Introduction, in *The Geologic Time Scale*, edited by F. M. Gradstein, J. G. O. D. Schmitz, and G. M. Ogg, chapt. 1, pp. 1–29, Elsevier, Boston, Mass., doi:10.1016/B978-0-444-59425-9.00001-9.
Grujic, D., I. Coutand, B. Bookhagen, S. Bonnet, A. Blythe, and C. Duncan (2006), Climatic forcing of erosion, landscape, and tectonics in the Bhutan Himalayas, *Geology*, *34*(10), 801–804.
Hansen, J., M. Sato, G. Russell, and P. Kharecha (2013), Climate sensitivity, sea level and atmospheric carbon dioxide, *Philos. Trans. R. Soc. A*, *371*, doi:10.1098/rsta.2012.0294.
Heermance, R., J. Chen, D. Burbank, and C. Wang (2007), Chronology and tectonic controls of Late Tertiary deposition in the southwestern Tian Shan foreland, NW China, *Basin Res.*, *19*(4), 599–632.
Helland-Hansen, W. (2010), Facies and stacking patterns of shelf-deltas within the Palaeogene Battfjellet Formation, Nordenskiöld Land, Svalbard: Implication for subsurface reservoir prediction, *Sedimentology*, *57*, 190–208, doi:10.1111/j.1365-3091.2009.01102.x.
Hirschmiller, J., D. Grujic, B. Bookhagen, I. Coutand, P. Huyghe, J.-L. Mugnier, and T. Ojha (2014), What controls the growth of the Himalayan foreland fold-and-thrust belt?, *Geology*, *42*, 247–250.
Hoorn, C., T. Ohja, and J. Quade (2000), Palynological evidence for vegetation development and climatic change in the Sub-Himalayan Zone (Neogene, Central Nepal), *Palaeogeogr. Palaeoclimatol. Palaeoecol.*, *163*(3), 133–161.
Hurford, A. J. (1990), Standardization of fission-track dating calibration: Recommendation by the Fission Track Working Group of the I.U.G.S. Subcommission on Geochronology, *Chem. Geol.*, *80*, 171–178.
Hurford, A. J., and P. F. Green (1983), The zeta age calibration of fission-track dating, *Isot. Geosci.*, *1*, 285–317.
Huyghe, P., J.-L. Mugnier, A. Gajurel, and B. Delcaillau (2005), Tectonic and climatic control of the changes in the sedimentary record of the Karnali River section (Siwaliks of Western Nepal), *Isl. Arc*, *14*, 311–327, doi:10.1111/j.1440-1738.2005.00500.x.

Hyne, N., W. Cooper, and P. Dickey (1979), Stratigraphy of intermontane, lacustrine delta, Catatumbo River, Lake Maracalbo, Venezuela, *AAPG Bull.*, *63*(11), 2042–2057.
International Committee for Coal and Organic Petrology (2001), The new vitrinite classification (ICCP Systems 1994), *Fuel*, *80*, 459–471.
Jain, V., and R. Sinha (2003), River systems in the Gangetic plains and their comparison with the Siwaliks: A review, *Curr. Sci.*, *84*(8), 1025–1033.
Jo, H., C. Rhee, and S. Chough (1997), Distinctive characteristics of a streamflow-dominated alluvial fan deposit: Sanghori area, Kyongsang Basin (Early Cretaceous), southeastern Korea, *Sediment. Geol.*, *110*, 51–79.
Johnson, G. D., N. D. Opdyke, S. K. Tandon, and A. C. Nanda (1983), The magnetic polarity stratigraphy of the Siwalik Group at Haritalyangar (India) and a new last appearance datum for Ramapithecus and Sivapithecus in Asia, *Palaeogeogr. Palaeoclimatol. Palaeoecol.*, *44*(3–4), 223–249.
Johnson, S., and A. Nur Alam (1991), Sedimentation and tectonics of the Sylhet trough, Bangladesh, *Geol. Soc. Am. Bull.*, *103*(11), 1513–1527.
Jordan, T. (1995), Retroarc foreland and related basins, in *Tectonics of Sedimentary Basins*, edited by C. Busby and R. Ingersoll, pp. 331–362, Blackwell Sci., Cambridge, Mass.
Kayal, J., S. Arefiev, S. Baruah, R. Tatevossian, N. Gogoi, M. Sanoujam, J. Gautam, D. Hazarika, and D. Borah (2010), The 2009 Bhutan and Assam felt earthquakes (M_w 6.3 and 5.1) at the Kopili fault in the northeast Himalaya region, *Geomatics Nat. Hazards Risk*, *1*(3), 273–281.
Kumar, R., S. K. Ghosh, R. K. Mazari, and S. J. Sangode (2003), Tectonic impact on the fluvial deposits of Plio-Pleistocene Himalayan foreland basin, India, *Sediment. Geol.*, *158*(3–4), 209–234, doi:10.1016/S0037-0738(02)00267-1.
Kumar, R., S. J. Sangode, and S. K. Ghosh (2004), A multistorey sandstone complex in the Himalayan foreland basin, NW Himalaya, India, *J. Asian Earth Sci.*, *23*(3), 407–426, doi:10.1016/S1367-9120(03)00176-7.
Lallier, F., C. Antoine, J. Charreau, G. Caumon, and J. Ruiu (2013), Management of ambiguities in magnetostratigraphic correlation, *Earth Planet. Sci. Lett.*, *371*, 26–36.
Lang, K., K. Huntington, R. Burmester, and B. Housen (2016), Rapid exhumation of the eastern Himalayan syntaxis since the late Miocene, *Geol. Soc. Am. Bull.*, *28*, 1403–1422, doi:10.1130/B31419.1.
Mallet, F. (1876), *On the Coal-Fields of the Naga Hills Bordering the Lakhimpur and Sibsagar Districts, Assam*, Geol. Surv. of India.
Marshall, J. (2000), Sedimentology of a Devonian fault-bounded braidplain and lacustrine fill in the lower part of the Skinkle Sandstones, Dyfed, Wales, *Sedimentology*, *47*, 325–342.
Mazurek, M., A. Hurford, and W. Leu (2006), Unravelling the multi-stage burial history of the Swiss Molasse Basin: Integration of apatite fission track, vitrinite reflectance and biomarker isomerisation analysis, *Basin Res.*, *18*(1), 27–50.
McCormick, D., and J. Grotzinger (1993), Distinction of marine from alluvial facies in the Paleoproterozoic (1.9 Ga) Burnside Formation, Kilohigok Basin, N.W.T., Canada, *J. Sediment. Petrol.*, *63*(3), 398–419.
McFadden, P., and M. McElhinny (1988), The combined analysis of remagnetization circles and direct observations in palaeomagnetism, *Earth Planet. Sci. Lett.*, *87*, 161–172.
McQuarrie, N., and T. Ehlers (2015), Influence of thrust belt geometry and shortening rate on thermochronometer cooling ages: Insights from thermokinematic and erosion modeling of the Bhutan Himalaya, *Tectonics*, *34*, 1055–1079, doi:10.1002/2014TC003783.
Mehrotra, R., N. Awasthi, and S. Dutta (1999), Study of the fossil wood from the upper Tertiary sediments (Siwalik) of Arunachal Pradesh, India and its interpretations in terms of palaeoecology, and phytogeographical interpretations, *Rev. Palaeobot. Palynol.*, *107*, 223–247.
Meigs, A. J., D. W. Burbank, and R. A. Beck (1995), Middle-late Miocene (>10 Ma) formation of the Main Boundary thrust in the western Himalaya, *Geology*, *23*(5), 423–426.
Miall, A. (1977), A review of the braided river depositional environment, *Earth Sci. Rev.*, *13*, 1–62.
Miall, A. (1985), Architectural-element analysis: A new method of facies analysis applied to fluvial deposits, *Earth Sci. Rev.*, *22*, 261–308.
Miller, D. S., I. R. Duddy, P. F. Green, A. J. Hurford, and C. W. Naeser (1985), Results of interlaboratory comparison of fission-track age standards, *Nucl. Tracks Radiat. Meas.*, *10*, 381–391.
Miller, K., M. Kominz, J. Browning, J. Wright, G. Mountain, M. Katz, P. Sugarman, B. Cramer, N. Christie-Blick, and S. Pekar (2005), The phanerozoic record of global sea-level change, *Science*, *310*, 1293–1298.
Mitra, S., and S. Mitra (2001), Tectonic setting of the Precambrian of the north-eastern India (Meghalaya Plateau) and age of Shillong Group of rocks, *Geol. Surv. India Spec. Publ.*, *64*, 653–658.
Mitra, S., K. Priestley, A. Bhattacharyya, and V. K. Gaur (2005), Crustal structure and earthquake focal depths beneath northeastern India and southern Tibet, *Geophys. J. Int.*, *160*(1), 227–248, doi:10.1111/j.1365-246X.2004.02470.x.
Molnar, P., and J. M. Stock (2009), Slowing of India's convergence with Eurasia since 20 Ma and its implications for Tibetan mantle dynamics, *Tectonics*, *28*, TC3001, doi:10.1029/2008TC002271.
Monga, P., M. Kumar, V. Prasad, and Y. Joshi (2015), Palynostratigraphy, palynofacies and depositional environment of a lignite-bearing succession at Surkha Mine, Cambay Basin, north-western India, *Acta Palaeobot.*, *55*(2), 183–207.
More, S., D. Paruya, S. Taral, T. Chakraborty, and S. Bera (2016), Depositional environment of Mio-Pliocene Siwalik sedimentary strata from the Darjeeling Himalayan Foothills, India: A palynological approach, *PLoS One*, *11*(3), e0150168.
Morley, R. (1991), Tertiary stratigraphic palynology in Southeast Asia: Current status and new directions, *Bull. Geol. Soc. Malays.*, *28*, 1–36.
Mugnier, J., E. Chalaron, G. Mascle, B. Pradier, and G. Herail (1995), Structural and thermal evolution of the Siwaliks of western Nepal, *J. Nepal Geol. Soc.*, *11*, 171–178.
Mugnier, J.-L., P. Huyghe, P. Leturmy, and F. Jouanne (2004), Episodicity and rates of thrust-sheet motion in the Himalayas (western Nepal), *Am. Assoc. Pet. Geol. Mem.*, *82*, 91–114.
Myrow, P., C. Lukens, M. Lamb, K. Houck, and J. Strauss (2008), Dynamics of a transgressive prodeltaic system: Implications for geography and climate within Pennsylvanian intracratonic Basin, Colorada, USA, *J. Sediment. Res.*, *78*, 512–528, doi:10.2110/jsr.2008.061.
Najman, Y. (2006), The detrital record of orogenesis: A review of approaches and techniques used in the Himalayan sedimentary basins, *Earth Sci. Rev.*, *74*(1), 1–72.
Najman, Y. (2007), Comment on "Biochronological continuity of the paleogene sediments of the Himalayan foreland basin: Paleontological and other evidences"–Bhatia, SB & Bhargava ON, 2006, JAES 26, 477–487, *J. Asian Earth Sci.*, *30*(2), 417–421.
Najman, Y., R. Allen, E. Willett, A. Carter, D. Barfod, E. Garzanti, J. Wijbrans, M. Bickle, G. Vezzoli, and S. Ando (2012), The record of Himalayan erosion preserved in the sedimentary rocks of the Hatia Trough of the Bengal Basin and the Chittagong Hill Tracts, Bangladesh, *Basin Res.*, *24*(5), 499–519.
Najman, Y., L. Bracciali, R. Parrish, E. Chisty, and A. Copley (2016), Evolving strain partitioning in the Eastern Himalaya: The growth of the Shillong Plateau, *Earth Planet. Sci. Lett.*, *433*, 1–9.
Nakayama, K., and P. D. Ulak (1999), Evolution of fluvial style in the Siwalik Group in the foothills of the Nepal Himalaya, *Sediment. Geol.*, *125*(3–4), 205–224.
Ojha, T., R. Butler, J. Quade, P. DeCelles, D. Richards, and B. Upreti (2000), Magnetic polarity stratigraphy of the Neogene Siwalik Group at Khutia Khola, far-western Nepal, *Bull. Geol. Soc. Am.*, *112*, 424–434.

Ojha, T., R. Butler, P. DeCelles, and J. Quade (2009), Magnetic polarity stratigraphy of the Neogene foreland basin of Nepal, *Basin Res.*, *21*, 61–90.
Olariu, C., and J. Bhattacharya (2006), Terminal distributary channels and delta front architecture of river-dominated delta systems, *J. Sediment. Res.*, *76*, 212–233, doi:10.2110/jsr.2006.026.
Plink-Björklund, P., and R. Steel (2006), Deltas on falling-stage and lowstand shelf margins, the Eocene Central Basin of Spitsbergen: Importance of sediment supply, in *River Delta - Concepts, Models, and Examples*, edited by L. Giosan and J. Bhattacharya, *SEPM Spec. Publ.*, 179–206.
Puigdefàbregas, C., J. Muñoz, and M. Marzo (1986), Thrust belt development in the eastern Pyrenees and related depositional sequences in the southern foreland basin, in *Foreland Basins*, *Spec. Publ.*, edited by P. Allen and P. Homewood, pp. 229–246, Int. Assoc. of Sedimentol, Oxford.
Quade, J., J. Carter, T. Ojha, J. Adam, and T. Harrison (1995), Late Miocene environmental change in Nepal and the northern Indian subcontinent: Stable isotopic evidence from paleosols, *Geol. Soc. Am. Bull.*, *107*(12), 1381–1397.
Rajendran, C., K. Rajendran, B. Duarah, S. Baruah, and A. Earnest (2004), Interpreting the style of faulting and paleoseismicity associated with the 1897 Shillong, northeast India, earthquake: Implications for regional tectonism, *Tectonics*, *23*, TC4009, doi:10.1029/2003TC001605.
Ramos, A., and A. Sopeña (1983), Gravel bars in low-sinuosity streams (Permian and Triassic, central Spain), in *Modern and Ancient Fluvial Systems*, edited by J. Collison and J. Lewin, *Int. Assoc. Sedimentol. Spec. Publ.*, 301–312.
Reimann, K.-U., and K. Hiller (1993), *Geology of Bangladesh*, 160 pp., Borntraeger, Berlin.
Reiners, P., and M. Brandon (2006), Using thermochronology to understand orogenic erosion, *Annu. Rev. Earth Planet. Sci.*, *34*(1), 419–466.
Retallack, G. (1988), Field recognition of paleosols, in *Paleosols and Weathering Through Geologic Time*, edited by J. Reinhardt and W. Sigles, *Geol. Soc. Am. Spec. Pap.*, 1–20.
Sanyal, P., S. Bhattacharya, R. Kumar, S. Gosh, and S. Sangode (2004), Mio-Pliocene monsoonal record from Himalayan Foreland basin (Indian Siwalik) and its relation to the vegetational change, *Palaeogeogr. Palaeoclimatol. Palaeoecol.*, *205*, 23–41.
Schlunegger, F., T. Jordan, and E. Klaper (1997), Controls of erosional denudation in the orogen on foreland basin evolution: The Oligocene central Swiss Molasse Basin as an example, *Tectonics*, *16*, 823–840, doi:10.1029/97TC01657.
Selvam, A., R. Prasad, R. Raju, and R. Sinha (1995), Rb-Sr age of the metaluminous granitoids of South Khasi Batholith, Meghalaya: Implications on its genesis and Pan-African activity in Northeastern India, *J. Geol. Soc. India*, *46*(6), 619–624.
Shukla, U., I. Singh, M. Sharma, and S. Sharma (2001), A model of alluvial megafan sedimentation: Ganga Megafan, *Sediment. Geol.*, *144*, 243–262.
Sinclair, H., and P. Allen (1992), Vertical versus horizontal motions in the Alpine orogenic wedge: Stratigraphic response in the foreland basin, *Basin Res.*, *4*(3–4), 215–232.
Singh, T., and S. Tripathi (1990), Siwalik sediments of the Arunachal Himalaya: Palynology, palaeoecology and palaeogeography, *Palaeobotanists*, *38*, 325–332.
Stockmal, G., D. Cant, and J. Bell (1992), Relationship of the stratigraphy of the Western Canada foreland basin to Cordilleran tectonics: Insights from geodynamic models, *Am. Assoc. Pet. Geol. Mem.*, *55*, 107–124.
Strecker, M., G. Hilley, B. Bookhagen, and D. Sobel (2012), Structural, geomorphic and depositional characteristics of contiguous vs. broken foreland basins: Examples from the eastern flanks of the central Andes in Bolivia and NW Argentina, in *Tectonics of Sedimentary Basins: Recent Advances*, edited by C. J. Busby and A. Azor, pp. 508–521, Blackwell, Oxford, U. K.
Suresh, N., S. Ghosh, R. Kumar, and S. Sangode (2004), Clay-mineral distribution patterns in late Neogene fluvial sediments of the Subathu sub-basin, central sector of Himalayan foreland basin: Implications for provenance and climate, *Sediment. Geol.*, *163*, 265–278.
Tauxe, L. (1998), *Paleomagnetic Principles and Practice*, 299 pp., Kluwer Acad., Dordrecht, Netherlands.
Tokuoka, T., K. Takayasu, M. Yoshida, and K. Hisatomi (1986), The Churia (Siwalik) Group of the Arung khola area, west central Nepal, *Mem. Fac. Sci., Shimane Univ.*, *20*, 135–210.
Tomlinson, P. (1994), *The Botany of Mangroves*, Cambridge Univ. Press, Cambridge.
Traverse, A. (1988), *Paleopalynology*, edited by N. H. Landman and D. S. Jones, 600 pp., Springer, Dordrecht, Netherlands.
Tye, R., and J. Coleman (1989), Depositional processes and stratigraphy of fluvially dominated lacustrine deltas: Mississippi delta plain, *J. Sediment. Petrol.*, *59*(6), 973–996.
van der Beek, P., X. Robert, J. Mugnier, M. Bernet, P. Huyghe, and E. Labrin (2006), Late Miocene—Recent exhumation of the central Himalaya and recycling in the foreland basin assessed by apatite fission-track thermochronology of Siwalik sediments, Nepal, *Basin Res.*, *18*(4), 413–434.
Verma, R., and M. Mukhopadhyay (1977), An analysis of the gravity field in northeastern India, *Tectonophysics*, *42*(2), 283–317.
Vermeesch, P. (2012), On the visualisation of detrital age distributions, *Chem. Geol.*, *312–313*, 190–194.
Vernant, P., R. Bilham, W. Szeliga, D. Drukpa, S. Kalita, A. Bhattacharya, V. Gaur, P. Pelgay, R. Cattin, and T. Berthet (2014), Clockwise rotation of the Brahmaputra Valley relative to India: Tectonic convergence in the eastern Himalaya, Naga Hills, and Shillong Plateau, *J. Geophys. Res. Solid Earth*, *119*, 6558–6571, doi:10.1002/2014JB011196.
White, N., M. Pringle, E. Garzanti, M. Bickle, Y. Najman, H. Chapman, and P. Friend (2002), Constraints on the exhumation and erosion of the High Himalayan Slab, NW India, from foreland basin deposits, *Earth Planet. Sci. Lett.*, *195*(1), 29–44.
Willis, B. (1993), Evolution of Miocene fluvial systems in the Himalayan foredeep through a two kilometer-thick succession in northern Pakistan, *Sediment. Geol.*, *88*(1–2), 77–121.
Wizevich, M. (1992), Sedimentology of Pennsylvanian quartzose sandstones of the Lee Formation, central Appalachian Basin: Fluvial interpretation based on lateral profile analysis, *Sediment. Geol.*, *78*, 1–47.
Worm, H.-U., A. Ahmed, N. Ahmed, H. Islam, M. Huq, U. Hambach, and J. Lietz (1998), Large sedimentation rate in the Bengal Delta: Magnetostratigraphic dating of Cenozoic sediments from northeastern Bangladesh, *Geology*, *26*(6), 487–490.
Xie, X., and P. Heller (2009), Plate tectonics and basin subsidence history, *Geol. Soc. Am. Bull.*, *121*(1–2), 55–64.
Yin, A., C. Dubey, A. Webb, T. Kelty, M. Grove, G. Gehrels, and W. Burgess (2010), Geologic correlation of the Himalayan orogen and Indian craton: Part 1. Structural geology, U-Pb zircon geochronology, and tectonic evolution of the Shillong Plateau and its neighboring regions in NE India, *Geol. Soc. Am. Bull.*, *122*(3–4), 336–359.
Zaleha, M. J. (1997), Intra- and extrabasinal controls on fluvial deposition in the Miocene Indo-Gangetic foreland basin, northern Pakistan, *Sedimentology*, *44*(2), 369–390, doi:10.1111/j.1365-3091.1997.tb01530.x.